# Chapter 11
# Phase Dynamics and Macroscopic Quantum Tunneling


**Davide Massarotti and Francesco Tafuri**

This chapter is dedicated to review concepts, theory and experimental results on whether and in which conditions a quantum system interacting with its environment can tunnel out of a metastable state. This will lead us to deal with macroscopic quantum tunneling (MQT), of great interest for the extrapolation of quantum mechanics to the macroscopic scale. Quantum mechanics survive at the macroscopic level through collective phenomena such as superfluidity, superconductivity, flux quantization and the Josephson effect. These phenomena are conventionally described as being "macroscopic", since they are manifestations on a macroscopic scale of the coherent addition of microscopic variables, each governed by quantum mechanics. As emphasized in Chap. 2, it is important to distinguish macroscopic quantum phenomena originating in the superposition of a large number of microscopic variables from those displayed by a single macroscopic degree of freedom, which is the main topic of this chapter.

Differently from the tunneling of a microscopic entity, coupling to the environment plays a major role in the macroscopic analog, and can be so strong that the motion in the classically accessible region is highly damped. The MQT experiments demonstrate that $\varphi$ is a quantum variable. Although a Josephson junction (JJ) contains a large number of atomic constituents, it is atom-like in the sense that it has a single degree of freedom behaving quantum mechanically. Thermal energy must be sufficiently low to avoid incoherent mixing of eigenstates, and the macroscopic degree of freedom must be sufficiently decoupled from other degrees of freedom for the lifetime of the quantum states to be long on the characteristic time scale of the system. The way the structure is biased and the amplitude of thermal and quantum fluctuations basically determine the way the Josephson effect manifests itself in an

D. Massarotti (✉) · F. Tafuri
Dipartimento di Fisica "E.Pancini", Universitá di Napoli Federico II, Complesso Universitario Monte Sant'Angelo Via Cinthia 26, 80126 Napoli, Italy
e-mail: davide.massarotti@unina.it

F. Tafuri
e-mail: francesco.tafuri@unina.it



F. Tafuri (ed.), *Fundamentals and Frontiers of the Josephson Effect*,
Springer Series in Materials Science 286,
https://doi.org/10.1007/978-3-030-20726-7_11

experiment. Differently from the phase-biased case occurring when the JJ is inserted in a superconducting loop, we will consider in this chapter always the case of a dissipative biased JJ using either an external voltage or a current source. We will evaluate the consequence of dissipation in studying the response of a JJ through I-V curves and switching current distributions (SCDs).

## 11.1 Escape Out of a Metastable State

A system with a one-dimensional degree of freedom $x$, described by a potential shape $V(x)$ similar to the washboard potential (see Fig. 11.1a), will escape out of the initial well state, where the system has been previously prepared, either by thermal activation over the barrier at higher temperatures, or by quantum tunneling at lower temperatures. An external bias field $F$ adds an energy term $-Fx$, and provides a convenient tool to study the escape process. By steadily ramping the field, the value of $F$ at which escape occurs, differs from run to run of the experiment because of the stochastic nature of the escape process. One needs to consider the entire distribution $P(F)$ of escape fields. In the case of a current-biased JJ, $x$ is the phase $\varphi$ and the bias field is the current $I$. The escape from this metastable state corresponds to the appearance of a finite voltage across the junction and the particle runs down the washboard potential.

### *11.1.1 Theoretical Background, Effects of Dissipation and the Underdamped Limit*

Escape rates are obtained by measuring the switching current distribution (SCD) from the S to the R branch in the I-V curves. More specifically, when ramping the bias current $I$ the tilt of the energy potential increases and the height

$$\Delta U(I) = 4\sqrt{2}/3 \cdot E_J(1 - I/I_c)^{3/2} \tag{11.1}$$

of the energy barrier between consecutive wells decreases (see Fig. 11.1a). Due to thermal fluctuations and quantum tunneling, the junction may switch to the finite voltage state for values of $I < I_c$. The relative weight of these two escape processes depends on the temperature of the system. For $k_BT >> \hbar\omega_J$ the escape process is dominated by Thermal Activation (TA) (see Fig. 11.1b) with a rate [1–3]:

$$\Gamma_T(I) = a_T \frac{\omega_J(I)}{2\pi} \exp\left(-\frac{\Delta U(I)}{k_BT}\right) \tag{11.2}$$

where the prefactor is $a_t = 4/[(1 + Qk_BT/1.8\Delta U)^{1/2} + 1]^2$.

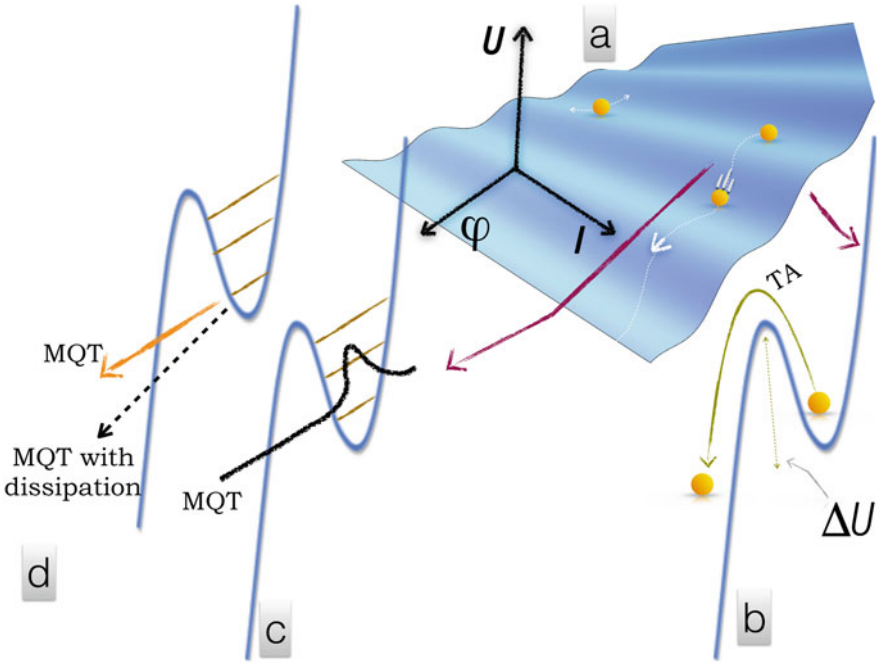


**Fig. 11.1** **a** 3-D view of the washboard potential as a function of different values of the bias current for the classical $I_s(\varphi)$ relation ($I_s = I_c \sin(\varphi)$). The phase overcomes the barrier in the washboard potential by Thermal Activation (TA) (**b**) or by Macroscopic Quantum Tunneling (MQT) (**c**), then it rolls in the running state. **d** MQT sketch in presence of dissipation

In thermal activation, the system is classical and is described by a classical equation of motion (1.49) representing a point particle -the phase- with a continuous range of energy. At lower temperatures (1.49) is no longer valid and the phase difference $\varphi$ must be represented by a quantum mechanical operator. The position is now described by a wave packet $\psi(\varphi)$ and the energy of the particle can assume only discrete values corresponding to the eigenstates of the system. The leakage of $\psi(\varphi)$ under the barrier represents the macroscopic quantum tunneling (MQT) (see Fig. 11.1c) of the phase $\varphi$. The crossover temperature [4] between TA and MQT regimes is indicated as $T_{cr}$ and will be extensively discussed in the experimental section of this chapter. The first calculation of the tunneling was made by Ivanchenko and Zil'berman [5] for a junction at $T = 0$ K with no dissipation. A major advance was made by Caldeira and Leggett (CL) [6–8], who proposed a model for quantum Brownian motion to incorporate the effect of the coupling to the environment. This model for velocity proportional to damping leads to a description in terms of an effective action containing non local terms, which imply an overall reduction in the tunneling rate. The effective action was calculated at $T = 0$ K and predicted an escape rate:

$$\Gamma_q(I) = a_q \frac{\omega_J(I)}{2\pi} \exp\left[-7.2\frac{\Delta U(I)}{\hbar\omega_J(I)}\left(1+\frac{0.87}{Q}\right)\right] \tag{11.3}$$

where $a_q = (864\pi\Delta U(I)/(\hbar\omega_J(I)))^{1/2}$. The effect of dissipation is the suppression of quantum tunneling by the factor depending on $Q$ [see (11.3)]. This can be also expressed in the physically more transparent form $exp[-A\eta(\Delta q)^2/\hbar]$ where $\Delta q$ is the "distance under the barrier" and $\eta$ the friction coefficient respectively. Dissipation narrows the wave packet and reduces $\Gamma_q(I)$. As a classical particle moves through a dissipative medium, a friction force proportional to the velocity of the particle arises. In our case of current-biased JJ described by the RSJ-like approach, the friction coefficient is physically due to the effective admittance $Y(\omega)$ shunting the JJ.

One of the effects of dissipation on the MQT process can be visualized in the scheme in Fig. 11.1d through a comparison with the MQT process in absence of dissipation [9]. Once the phase particle gets over a hill by fluctuations, it keeps running, provided that the damping is below some critical value. The transition to the running state only occurs if the kinetic energy gained by the phase particle running down the tilted washboard potential is not all dissipated, but enough energy remains to carry the phase over the next hill. This occurs if the junction is in the underdamped regime ($Q >> 1$).

Later works have extended the CL approach and modeled dissipation through a quantum-mechanical description of an effective shunt resistance in a JJ [10–14]. The tunneling of quasiparticles has been for instance described on the basis of the microscopic theory [10–12]. The linear dissipation and the Gaussian noise in CL have been replaced by dissipation due to single-electron tunneling and shot noise [10]. In [14] three different cases of effective shunt resistance have been studied: impurity scattering in a normal metal, transport through an orifice and tunneling in a junction, all producing in the classical limit an Ohmic resistance (ignoring the influence of a gap $\Delta$), but with a different effective action in the general quantum description. In the case of a microscopic Hamiltonian of conduction electrons in a dirty metal, for instance, the same action of the CL approach has been found, while a different action has been found in case of a short constriction between two metals [14].

How dissipation affects the probability for the particle (phase) to tunnel through the barrier has been solved at finite temperature $T$ [12, 13, 15, 16]. Well below $T_{cr}$, Grabert, Weiss and Hanggi have found an enhancement of $\Gamma(T)$ when compared with $T = 0$ rate reported above, according to the power law $\ln[\Gamma(T)/\Gamma_q] = \sigma_{GWH}T^2$, where $\sigma_{GWH}$ is proportional to $Y(\omega)$ [13]. This enhancement is physically due to the thermal current noise generated at low frequencies by the shunt admittance across the junction [13]. At higher $T$ corrections to $\ln[\Gamma(T)/\Gamma_q(0)]$ were found of the order of $(T/T_{cr})^4$, due to fast current fluctuations to which the phase difference $\varphi$ cannot adjust adiabatically [15].

Both ohmic and non-ohmic damping have been considered. Waxman and Leggett have used a density matrix for the description of the metastable state and obtained a contour of crossover between quantum and classical escape in the temperature – damping plane [16].

The escape-field distribution is related to the escape rate $\Gamma(F)$ by the following argument [17–19]. If $F$ is ramped from $F = 0$ at $t = 0$ at a steady rate $dF/dt$, the probability $W(F(t))$ that the systems will persist in the metastable state up to time $t$ is given by:

$$W(F(t)) = exp\Big[ - \int_0^t \Gamma(F(t'))dt' \Big] \tag{11.4}$$

Changing the variable of integration from $t'$ to $F(t')$, we obtain:

$$P(F) = -\frac{d}{dF} W(F) = \frac{\Gamma(F)}{dF/dt} exp\Big[ - \int_0^F \frac{\Gamma(F')}{dF/dt} dF' \Big] \tag{11.5}$$

When the escape field is the current, (11.5) turns into:

$$P(I) = \frac{\Gamma(I)}{dI/dt} \exp\left[ - \int_0^I \frac{\Gamma(I')}{dI'/dt} dI' \right]. \tag{11.6}$$

In a current-biased junction, the appearance of a voltage signals the escape of the particle from the well. A ramp is applied and the current value for which the voltage appears is measured for a large number of times, and finally collected in a histogram representing the escape probability versus bias current. From the distribution it is possible to derive the escape probability versus bias current. In a current-biased junction case, escape rate can be expressed as [18]:

$$\Gamma(I) = \frac{1}{\Delta I} \frac{dI}{dt} \ln \left( \frac{\sum_{i \geq I} P(I)}{\sum_{i \geq I + \Delta I} P(I)} \right) \tag{11.7}$$

where $dI/dt$ is the current ramp rate and $\Delta I$ is the current bin size.

The first two moments of the escape field distribution (mean and width) have been the common references for all experiments, where the self-consistent determination of all junction parameters in the classical regime is of crucial importance also in the quantum regime. Garg has calculated the first two moments of the escape field distribution for a particle in a steadily ramped potential and compared results from literature, where the escape rate can always be traced back to the form [19]:

$$\Gamma(\epsilon) = A\epsilon^{a+b-1} exp(-B\epsilon^b). \tag{11.8}$$

The quantities $A$, $B$, $a$ and $b$ depend on whether the escape is quantum or thermal, and the degree and type of damping, and $\epsilon$ is the reduced bias field $= 1 - F/F_c$ (for a current biased JJ $\epsilon = 1 - I/I_c$).

In literature a convenient way to express escape rates in both classical and quantum regimes is through an escape temperature $T_{esc}$ defined by the relation [29, 30]:

$$\Gamma = \frac{\omega_J(I)}{2\pi} \exp\left(-\frac{\Delta U}{k_B T_{esc}}\right) \tag{11.9}$$

In the classical regime $T_{esc}$ is very close to $T$, while in the quantum regime is temperature-independent.

### 11.1.2 The First Experiments

The first detailed measurements on thermal escape at $T \gg T_{cr}$ were made on a junction in a superconducting loop [17, 20] and on a current-biased junction [18], respectively. The width of the distribution was found to be proportional to the inductance of the ring and varying as $T^{2/3} I_c^{-1/3}$ in [17].

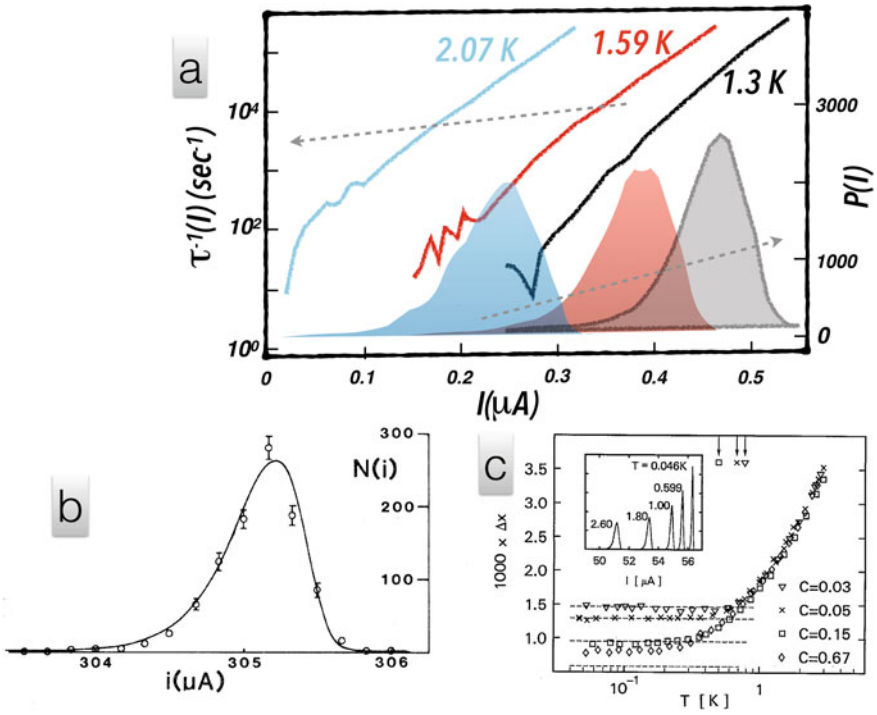


**Fig. 11.2** **a** SCDs and $log_{10}\tau^{-1}$ versus $I$ for a Sn-SnO-Sn junction. Adapted from [18]. **b** Measured distribution for high current density Pb-Pb(In) junctions ($J_c$ ranging from $5 \times 10^3$ A/cm$^2$ to $5 \times 10^5$ A/cm$^2$). From [22]. **c** Temperature behavior of the widths of SCDs for several junction capacitances. The arrows at the top are the predicted $T_{cr}$ for the first three junctions. The inset contains SCDs measured as a function of the temperature for $C = 0.15$ pF. From [26]

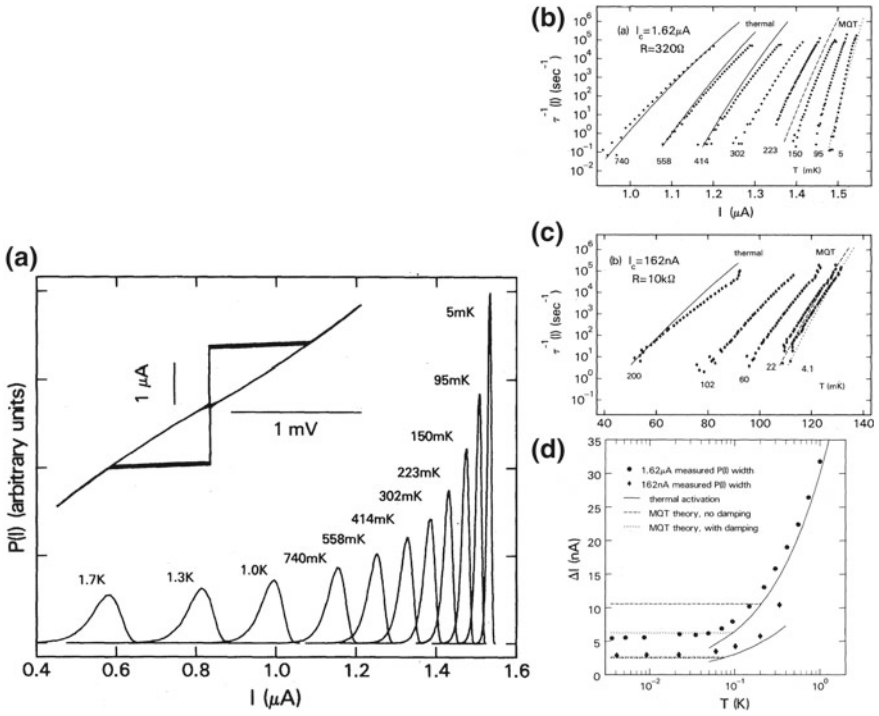


**Fig. 11.3** **a** SCDs versus $I$ for a 1 μm Nb junction for different temperatures $T$. In the inset the I-V curve is measured at 95 mK ($\beta_c = 50$, $C = 0.1$ pF). Transition rates are derived from SCDs for two junctions with $I_c \approx 1.62\,\mu$A, $R_n \approx 320\ \Omega$ (**b**) and $I_c \approx 162$ nA, $R_n \approx 10$ kΩ (**c**) respectively. Theoretical thermal rates are shown as solid lines, MQT without damping as dashed lines, with damping as dotted lines. **d** Measured widths of the SCDs as a function of $T$ for the two junctions. The higher $I_c$ sample shows reduced tunneling rates due to dissipation. From [21]

The very first experiments to measure MQT in a JJ were carried out by by Voss and Webb [21] and by Jackel et al. [22], while related experiments on a junction inserted in a superconducting loop were realized by de Bruyn Ouboter et al. [23], Prance et al. [24] and Dmitrenko et al. [25]. The temperature dependence of the effect of damping on the tunneling was addressed in later experiments [26, 27]. In Figs. 11.2 and 11.3, we report a collection of some of these first SCD measurements, realized on different types of junctions with different parameters.

In all these experiments the behavior of the phase difference $\varphi$ was deduced from measurements of the escape rate $\Gamma$ of the junctions from its zero-voltage state as described above. To determine the escape rate $10^4 - 10^5$ events were typically collected for each set of parameters. The measurement technique for most of the SCD measurements described in this chapter consists in ramping the bias current at a constant sweep rate (typically in the range between a few hundreds of μA/s and a few tens of mA/s). The voltage is measured by using a low noise differential

amplifier and is fed into a threshold detector which is set to generate a pulse signal when the junction switches from the superconducting state to the finite voltage state. This signal is used to record the value of the switching current. An alternative method consists in fixing a bias current $I < I_c$ applied to the junction at an initial time $t$ and measuring the time delay $\Delta t$ until a voltage across the junction appears [28]. From statistical distribution of the measured times $\Delta t$, the lifetime $\tau(I)$ of the junction in the zero-voltage state can be determined. The inverse of the lifetime corresponds to the escape rate $\Gamma(I)$. A detailed discussion on the design of these types of experiments and on the requirements of the experimental probes, from room temperature and cryogenic filters to ground connections and electronic setup, can be found in various of the manuscripts mentioned above and in [28–36]. Martinis et al. [30] stays as a milestone in the field.

In these experiments the escape rate tended to become constant as the temperature was lowered and to be reduced as the dissipation was increased. For all of them, the difficulty has been the lack of knowledge of the junction parameters in the relevant microwave frequency range. Devoret, Martinis and Clarke have neatly demonstrated MQT and energy level quantization (ELQ) relying on an accurate experimental procedure to use classical phenomena to measure junction parameters in situ, ranging from $I_c$ to $C$ and $R_n$ [29–31], and addressing the problem of the complex impedance seen by the junction at microwave frequency due to the wires directly connected to it or by any circuit in its vicinity. This was fundamental to compare experiments with theory in the quantum regime with no adjustable parameters. A detailed account of the procedure is given in [30].

Through resonant activation (RA) the parameters $\omega_J(I)$ and $Q(I)$ were first determined [30, 31]. RA deals with the enhancement of the escape rate by a microwave current applied to the junctions. For a microwave frequency close to $\omega_J$, the particle is raised to a state of higher energy with an increase of the probability of overcoming the barrier. The enhancement in the escape rate is asymmetric in frequency, with a rapid fall off at higher frequencies and a long tail on the low frequency side, as a consequence of the anharmonicity of the potential well. By using numerical simulations of the Brownian motion in presence of a weak sinusoidal force [30], $\omega_J(I)$ and $Q(I)$ can be determined from this resonant effect.

The measurement of the escape rate in the absence of microwaves $\Gamma(0)$ allows to determine $I_c$. By inserting the expression of (11.1) in (11.2), the quantity $[\ln[\omega_J(I)/(2\pi\Gamma(I))]]^{2/3}$ depends linearly on $I$ with a slope scaling as $T^{2/3}$ and with an intercept with the current axis very close to $I_c$. Once determined $I_c$ and $\omega_J(I)$, from the relation $\omega_J(I) = (2eI_c/\hbar C)^{1/2}(1 - I/{I_c}^2)^{1/4}$ it is possible to infer $C$ [30].

The value of $I_c$ obtained from the temperature dependence of $\Gamma(I)$ is considerably more accurate than the value obtained from RA, but this slight difference does not have any effect on the revised value of $C$. Finally $R$ is extracted from (1.51). The error in $I_c$ is the standard deviation arising from statistical uncertainties. The errors in $C$ and $R$, which arise from the fact that these quantities vary with bias current and thus with frequency, as shown in Fig. 11.4b, c, are a measure of the departure of the junction and its leads from the simple RSJ model [30]. In [28–31], the fractional error in $C$ was

**Table 11.1** Junction parameters of the first experiments on the macroscopic quantum tunneling of the phase $\varphi$ in an isolated Josephson junction, as reported in the respective papers

| Reference | Junction | $I_c$ ($\mu A$) | C (pF) | R ($\Omega$) | Q | $T_{cr}$ (mK) |
|---|---|---|---|---|---|---|
| [21] | Nb/NbO$_x$/Nb | 1.62 | 0.1 | 320 | 7 | 100 |
| [21] | Nb/NbO$_x$/Nb | 0.16 | 0.1 | 10 k | 70 | 70 |
| [26] | Nb/Nb$_2$O$_5$/Nb | 55 | 0.05 | 23 | 2 | 750 |
| [26] | Nb/Nb$_2$O$_5$/Nb | 57 | 0.15 | 23 | 3.6 | 550 |
| [30] | Nb/NbO$_x$/PbIn | 9.49 | 6.35 | 190 | 30 | 30 |
| [31] | Nb/NbO$_x$/PbIn | 24.87 | 4.28 | 9.3 | 1.77 | 40 |

For the errors in the evaluation of the parameters, we refer to the text and to the original papers

small because the self-capacitance was chosen as large as possible to minimize the effects of the leads. The fractional error in $R$ was large, but in case of weak damping the effect of $Q$ on the MQT rate is small and the large variations in $R$ do not lead to large errors in the prediction of $T_{esc}$. In case of moderate damping different approaches are pursued to determine the $Q$ factor, as shown in Sect. 11.2. In [28–31], the measured value of $R$ was at least one order of magnitude less than the resistance $R_n$ of the junction measured from the static I-V characteristics. This points to a dissipation substantially determined by the bias circuitry [28–31]. Thus the self-capacitance of the junction was dominating on the shunting capacitance, while the bias circuitry on the shunting conductance respectively. Most of the parameters are collected in Table 11.1 [30, 31] and compared with those extracted from other experiments. These considerations need to be taken into account for a proper design of the junction and of its parameters, chosen to preserve quantum effects: $\hbar\omega_J \gg k_B T$ (no incoherent mixing of quantum state) and $R \gg Z_O = (L/C)^{1/2}$ (level width smaller than level separation, with $R$ representing the resistance due to the generic coupling to the environment and $Z_O$ the impedance of the quantum system) [30]. Further insights on dissipation in underdamped junctions can be found in [3, 37–43] and more will be discussed in Sect. 11.2.

$T_{esc}$ can be calculated as a function of $T$ on the basis of (11.9) though the determined values of $I_c$, $C$ and $R$. $T_{esc}$ is plotted as a function of bath temperature $T$ in Fig. 11.4d [30]. At temperatures above 100 mK, the values of $T_{esc}$ are very close to the bath temperature as expected in the thermal regime. As a direct consequence of the temperature independent behavior of $\Gamma$ and of the width of the SCDs, $T_{esc}$ is independent of $T$ below 25 mK, which represents in this case the crossover temperature $T_{cr}$ between the thermal regime at higher temperatures and the quantum regime at lower temperatures.

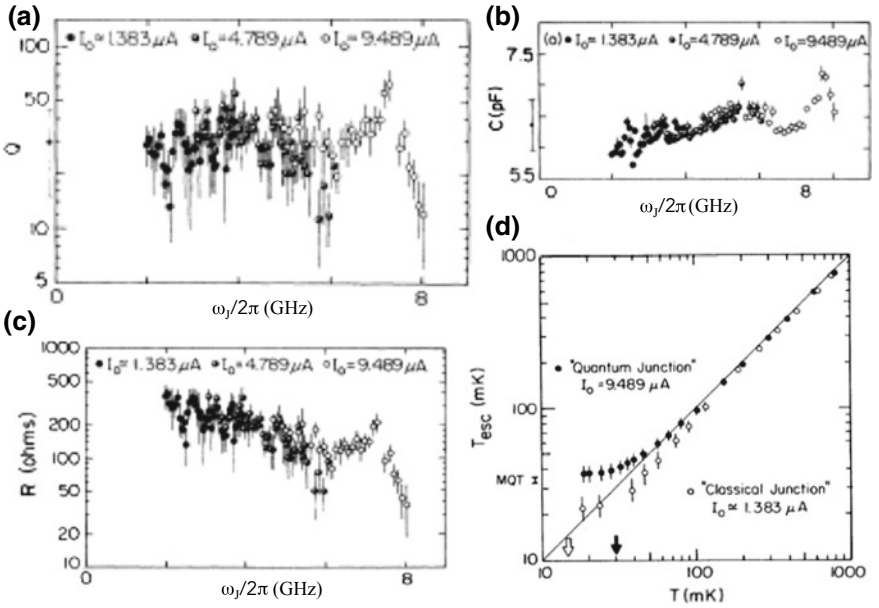


**Fig. 11.4** **a** $Q$ is reported as a function of $\omega_J$. As for **b** and **c** the possibility to modulate the critical current of the junction, indicated in this case by $I_o$, through an external magnetic field $H$, gives the opportunity of spanning a larger range of the plasma frequency. **b** $C$ is reported as a function of $\omega_J$. **c** $R$ is reported as a function of $\omega_J$ and is obtained from the measurement reported in (**a**). **d** $T_{esc}$ is reported as a function of bath temperature $T$ at $\ln(\omega_J/(2\pi\Gamma)) = 11$ for two different values of $I_o$. The smaller value of $I_o$ is obtained by applying an external magnetic field. A reduction of $I_o$ determines a lowering of $T_{cr}$, from the black to the white arrow. From [30]

### *11.1.3 The Effect of the Magnetic Field on SCD*

Despite the good agreement with predicted crossover temperature and the self-consistency of the whole set of the junction parameters, an additional in-situ knob is required to rule out the presence of spurious noise effects on the saturation of the measured $\Gamma$ values. The magnetic field $H$ has been successfully used to tune $T_{cr} = (\hbar\omega_J/2\pi k_B)\left\{\left(1 + 1/4Q^2\right)^{1/2} - 1/2Q\right\}$ [4]. $H$ modifies $I_c$ and as a consequence the plasma frequency $\omega_J$, thus tuning $T_{cr}$ (white arrow in Fig. 11.4d). When $I_c$ is further reduced by a magnetic field to leave the junction in the thermal regime at low temperatures, $\Gamma$ follows the predictions of the thermal model [29, 30].

In this and all other later experiments which used this procedure, the phenomenon of MQT is considered for a "point-like" JJ, i.e., completely neglecting the finiteness of the junction size $L$. This (zero order in $L$) approximation is based on the assumption that the junction size is much smaller than all other related parameters of the problem such as the Josephson penetration depth [44]. It was demonstrated that the effects due to the junction's size result in the appearance of a strong sensitivity of the MQT process on $H$, making $T_{cr}$ a non-monotonic function of $H$ [44].

### 11.1.4 Notes on Resonant Activation and Quantized Energy Level

In the quantum regime below $T_{cr}$, RA was also used to demonstrate spectroscopically the existence of quantized energy levels in the potential well of the junction [29, 30]. $\Gamma_0$ and $\Gamma_1$ indicate the tunneling process from the ground state and the first excited state respectively. When the microwave frequency $\Omega$ corresponded to the energy difference between these adjacent energy levels, tunnel can occur from the first excited state (see Fig. 11.5a–c). The discrete Lorentzian-shaped resonances observed as a function of the bias current are characteristic of the transitions between quantized energy levels in the well (see the sketch in Fig. 11.5d) and each transition has a distinct frequency due to the anharmonic nature of the well. In [29, 30], the position of the energy levels agreed quantitatively with quantum-mechanical predictions involving junction parameters measured in the thermal regime. The transition may involve more than one photon at once, thus called multi-photon transition, which has been observed experimentally as discussed below [45].

In Chap. 12 these measurements will be described in some detail. In Fig. 11.6a we give an example just to complete the general picture. Escape rates in normalized units ($[\Gamma(P) - \Gamma(0)]/\Gamma(0)$) in presence of microwaves at a fixed power $P$ and at 2 GHz are reported as a function of the current $I$ at $T = 28$ mK [30]. The microwave power was chosen so that the enhancement $\Gamma(P)/\Gamma(P = 0)$ was linear in $P$ [30]. Arrows indicate the current values at which the resonances occur. In the inset the corresponding transitions between energy levels are reported. These calculated energy-level spacings are reported in Fig. 11.6b. $[\Gamma(P) - \Gamma(0)]/\Gamma(0)$ versus $I$ is reported for different values of $k_B T/(\hbar\Omega)$ in Fig. 11.6c. This measurement represents the evolution from quantum to classical behavior as the ratio $k_B T/(\hbar\Omega)$ increases. At the lowest temperature (curve c, 3.7 GHz) a single Lorentzian - shaped resonance corresponding to the $0 \rightarrow 1$ transition is observed. At the intermediate temperature (curve b, 4.1 GHz), the thermal population of the first excited state is significant, and the shoulder at lower currents implies occurrence of $1 \rightarrow 2$ transition. At the highest temperature (curve a, 4.5 GHz), a broad asymmetric resonance occurs, signifying several closely spaced levels in the well. The individual transitions overlap, forming a continuous response, reminiscent of classical resonant activation [30]. Problems related to the distinction between quantum and classical limits of the macroscopic system have been also raised [46].

In [45] in the escape process of a Nb/Al-$AlO_x$/Nb junction in presence of microwave radiation in the frequency range between 10 and 38 GHz, both single photon and multiphoton transitions between the junction energy levels have been found. The different transitions are illustrated in Fig. 11.7b based on the numerical calculated energy levels reported in Fig. 11.7a. 3D plot of the measured SCDs versus the applied microwave power $P_{\mu w}$ at a frequency $\nu$ of 36.554 GHz and $T = 100$ mK are reported in Fig. 11.7c, along with the experimental escape rate for single-photon and two-photon absorption in Fig. 11.7d respectively. Multiphoton transitions can be related to the presence of resonant peaks at similar or at the same bias current for

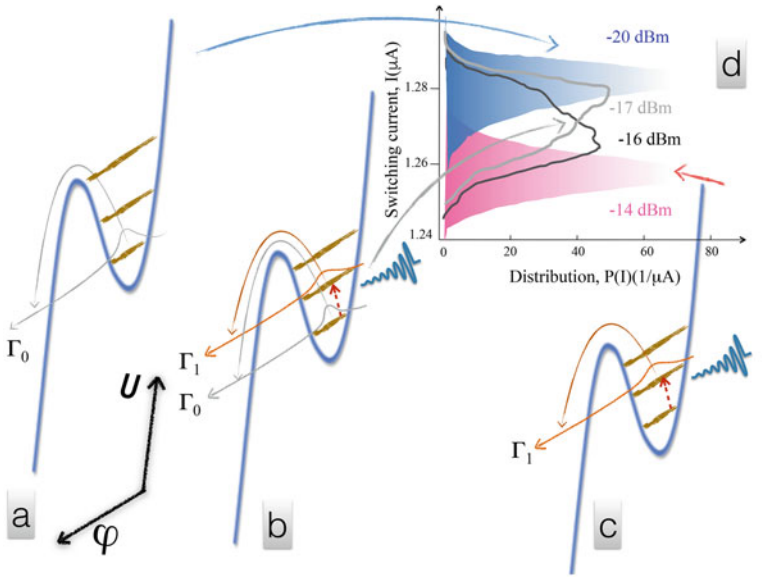


**Fig. 11.5** Detail of the washboard potential in the RSJ model in presence of microwaves. $\Gamma_0$ and $\Gamma_1$ indicate the tunneling process from the ground state and the first excited state, respectively. When the microwave frequency $\Omega$ corresponded to the energy difference between these adjacent energy levels, tunnel can occur from the first excited state. The anharmonic nature of the well, which results from the nonlinear inductance of JJs, causes the energy spacing to decrease as the quantum number progressively increases, so each transition has a distinct frequency. In **a** only the ground state is populated, in **b** both the ground state and the first excited state are populated, while in **c** the occupation probability is comparable (50% each), but the escape from the first excited state is exponentially faster and dominates. In **d** the SCDs are reported for these different configurations

very different microwave frequencies, as reported in Fig. 11.7e. In this experiment the junction parameters are: $J_c \approx 1.1.\,\mathrm{kA/cm^2}$, effective capacitance $C \approx 1.6$ pF and a subgap $R$ larger than 500 Ω.

An attempt to incorporate the phenomenon of Euclidean resonance (ER) into the quantum physics of JJs has been reported in [47]. ER is an extremely multiphoton phenomenon which occurs in two steps. The first step is fast, involving the time scale $\hbar/E_J$ when an outgoing wave packet is formed. In the second step, the wave packet moves slowly from under the barrier as a classical particle [47]. The method of classical trajectories in imaginary time allows to bypass the complicated dynamic region where the packet is created. The decay probability of a zero voltage state is predicted to display a peak at the certain *dc* resonant bias current. This current is not necessarily close to $I_c$ and depends on the amplitude and frequency of the *ac* component of the bias current. The adiabatic condition $\tilde{\tau} < \hbar/E_J$ corresponds to $I_c < 2e/\tilde{\tau}$. Therefore, materials with shorter relaxation times enable this type of experiments at much higher current [47].

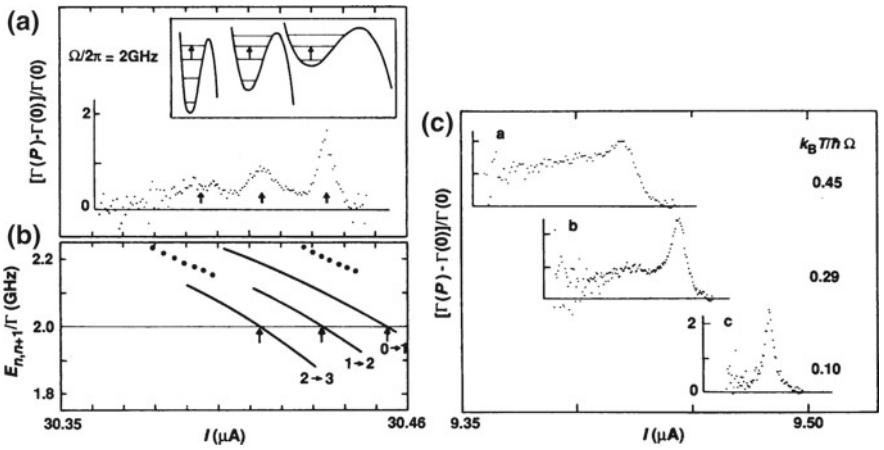


**Fig. 11.6** **a** Escape rates in normalized units ($[\Gamma(P) - \Gamma(0)]/\Gamma(0)$) in presence of microwaves at a fixed power $P$ and at 2 GHz are reported as a function of the current $I$ at $T = 28$ mK. Arrows indicate the current values at which peaks of the resonances occur. In the inset the corresponding transitions between energy levels are reported. **b** Energy-level spacings are calculated for the measurement reported in (**a**). **c** $[\Gamma(P) - \Gamma(0)]/\Gamma(0)$ versus $I$ is reported for different values of $k_B T/(\hbar\Omega)$ showing the evolution from quantum to classical behavior as the ratio $k_B T/(\hbar\Omega)$ increases. From [30]

### *11.1.5 The Master Equation for Phase Dynamics*

An understanding of the spectral line-widths and line-shifts has been crucial to interpret the experiments described above. The stationary solution of the master equation developed by Larkin and Ovchinnikov [48, 49]

$$\frac{\partial \rho_j(t)}{\partial t} = \sum_k \left[ w_{j\leftarrow k}\rho_k(t) - w_{k\leftarrow j}\rho_j(t) \right] - \gamma_j \rho_j(t) \qquad k = 0, \ldots, n \qquad (11.10)$$

has shown how in the weak-dissipation limit it is important to take into account the discrete structure of the levels within the potential well in calculating the lifetime of the metastable states. Here $\rho_j(t)$ is the probability for the particle to occupy the state $|j>$ at time $t$, $w_{j\leftarrow k}$ is the probability per unit time that the particle makes a transition from state $|k>$ to state $|j>$, and $\gamma_j$ is the rate for tunneling out of the metastable well from state $|j>$. $\gamma_j$ is obviously affected by dissipation. The time-dependent solution of the master equation gives the possibility to study the dependence of the lifetime of the particle inside the well on its initial probability distribution over the quantized energy levels [50]. This solution is fundamental to study non-equilibrium situations, and has been used in the interpretation of several experiments [45, 51, 66].

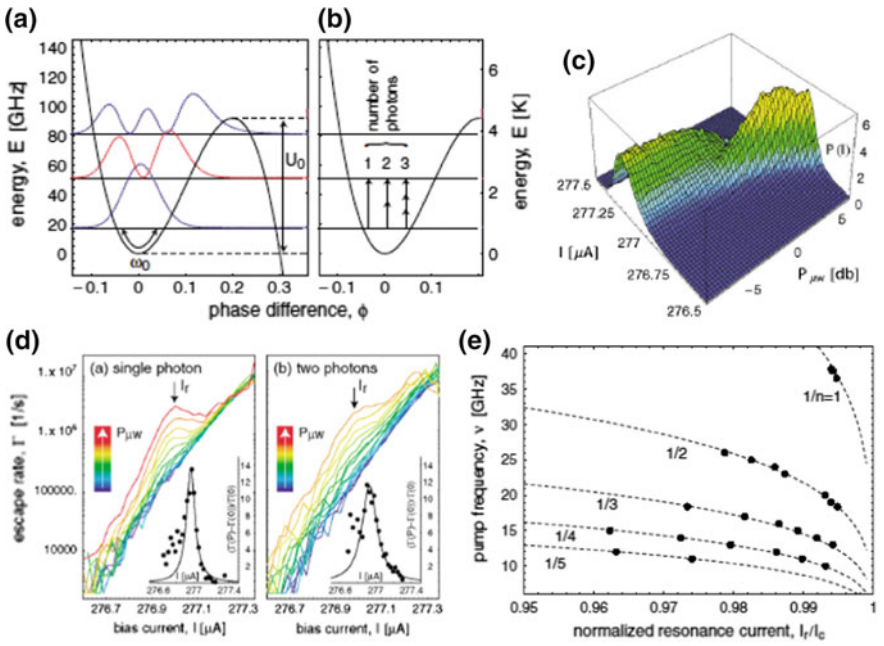


**Fig. 11.7** **a** Numerically calculated energy levels (dotted lines) and the squared wave functions (dashed lines) are shown. **b** Multiphoton transitions between the ground state and the first excited state. **c** 3D plot of the measured SCDs versus the applied microwave power $P_{\mu w}$ at a frequency $\nu = 36.554\,\text{GHz}$ and $T = 100\,\text{mK}$. **d** Experimental escape rate for single-photon and two-photon absorption. Different curves correspond to increasing microwave power $P_{\mu w}$. The resonance current $I_r$ is indicated by an arrow. The insets show the enhancement of the escape rate $[\Gamma(P_{\mu w}) - \Gamma(0)]/\Gamma(0)$ at the largest displayed value of $P_{\mu w}$. Symbols are data, solid lines are fits to a Lorentzian line shape. **e** Applied microwave frequency versus normalized resonant bias current $I_r/I_c$. From [45]

### *11.1.6 The Retrapping Current*

The retrapping or return current as introduced in Chap. 7 is another revealing feature of the junction dynamics and especially of the damping levels. While the escape rate in the TA and MQT regimes does not depend or is weakly affected by the damping parameter, see (11.2) and (11.3) respectively, the retrapping process is strongly dependent on dissipation. The analytical expression for the retrapping rate is given by [52]:

$$\Gamma_r(I) = \omega_J \frac{I - I_r}{I_c} \left( \frac{E_J}{2\pi k_B T} \right)^{1/2} \exp\left[ -\frac{E_J Q^2}{2k_B T} \left( \frac{I - I_r}{I_c} \right)^2 \right] \tag{11.11}$$

where $I_r \approx 4I_c/(\pi Q)$ is the retrapping current, as already introduced in Sect. 7.3.1. The relationship between the junction parameters and the histogram of the return

current values has been studied by Ben-Jacob et al. in the thermal regime [52], and by Chen, Fisher, and Leggett (CFL) in both thermal and quantum regimes under the condition $I - I_r \ll I_r$ [53].

Ben-Jacob et al. have calculated the lifetime $\tau_i$ of the non-equilibrium running state until it undergoes a transition to the zero-voltage equilibrium state [52]. The dynamic equation they find is similar in form to that obtained by Kramers to describe the transition from a stable equilibrium state, although the two processes are very different. The $\tau_i$ expression derived in [52] is the escape rate reported in (11.11), that once inserted into (11.6) allows to obtain the distribution of the retrapping currents.

CFL [53] give a deterministic evaluation of the I-V characteristics in the return region as discussed in Sect. 7.3.1, and of its statistical properties. Kirtley et al. have found that the current from which the high quality Nb-PbAuIn edge junctions switch from the voltage state into the zero-voltage state, is controlled by thermally excited quasiparticle tunneling [40]. Dissipation is in agreement with the CFL theory [40]. Castellano et al. [41] have measured the return current in Nb/$AlO_x$/Nb JJs. While the deterministic behavior, experimentally measured through the I-V curve, appears to be in agreement with the theoretical predictions, the statistical behavior is strongly different from what is expected even in zero-applied magnetic field. The effective resistance derived through statistical behavior was found to be higher by about a factor 10, leading to an unexpectedly low dissipation factor.

### *11.1.7 Thermal Activation and Macroscopic Quantum Tunneling in SQUIDs and Annular Junctions*

In this section we collect a few notions on TA and MQT specific of SQUIDs and annular junctions, i.e. in systems where flux due to magnetic field has an influence on the SCD measurements and the derived escape rates. A detailed account of the thermally and MQT activated escape rate out of the zero-voltage state of hysteretic dc SQUIDs can be found in [54–60]. The dc SQUID is described by two degrees of freedom, the phase differences across the two junctions $\varphi_1$ and $\varphi_2$ respectively, coupled through the loop inductance. The dynamics of the system can be studied by using the equation of motion of a particle, of mass proportional to the capacitance, moving in a two-dimensional potential given by:

$$U = -\Phi_o/(2\pi)\Bigg(Ix + 2I_c\cos(x)\cos(y) + 2I_c\alpha_{sq}\sin(x)\sin(y) + \\ + \eta_{sq}Iy - \frac{\Phi_o}{\pi L}\Big(y - \pi\Phi_{ext}/\Phi_o\Big)^2\Bigg) \quad (11.12)$$

where $x = (\varphi_1 + \varphi_2)$, $y = (\varphi_1 - \varphi_2)/2$, $\alpha_{sq}$ is the SQUID asymmetry parameter for the critical current (the two junctions have critical current $I_c(1 + \alpha_{sq})$ and $I_c(1 - \alpha_{sq})$ respectively), and finally $\eta_{sq}$ takes into account the asymmetry in the inductance of the

two branches ($L_2 - L_1 = \eta_{sq}L$) [57]. The 2D potential system is more complicate but has the advantage of being tunable and thus more flexible. In more than one dimension, escape can occur through infinitely many trajectories. There is, however, an optimal trajectory, which is the trajectory that passes through the saddle point with the lowest potential energy [57]. In the expressions of the TA ($\Gamma_{Tsq}$) and MQT ($\Gamma_{qsq}$) escape rates,

$$\Gamma_{Tsq}(I) = \frac{\omega_J(I)}{2\pi}\frac{\omega_{w\perp}}{\omega_s\perp}\exp\left(-\frac{\Delta U(I)}{k_B T}\right) \tag{11.13}$$

and

$$\Gamma_{qsq}(I) = f_{2D}(\alpha, \alpha_c)a_q\frac{\omega_J(I)}{2\pi}\exp\left[-7.2\frac{\Delta U(I)}{\hbar\omega_J(I)}\left(1+\frac{0.87}{Q}\right)\right] \tag{11.14}$$

new parameters will appear [58–60]. $\Delta U(I)$ is the potential-energy difference between the bottom of the well and the optimal saddle point, $\omega_{w\perp}$ and $\omega_s\perp$ (in the 2D case) are the angular frequencies of the modes perpendicular to the escape trajectory at the bottom of the well and at the saddle point, respectively, influencing the attempt frequency, $f_{2D}(\alpha, \alpha_c)$ is a dimensionless function of $\alpha$ and $\alpha_c$, where $\alpha$ is a measure of interaction between the two degrees of freedom and $\alpha_c$ is the critical parameter for instanton splitting [58]. Both $\Delta U$ and $\omega_J$ depend on the external magnetic field and on a possible asymmetry in the critical currents of the two junctions composing the SQUID. The SQUID can be also inserted into another loop with larger inductance, as a combined rf-dc SQUID [56]. This kind of geometry as discussed in Chap. 17 has been of inspiration for the design of qubit cells.

In [55] a crossover from TA escape to MQT was observed at a flux-dependent temperature for SQUIDs based on Pb-alloy window junction technique. While in this work Sharifi et al. [55] report on thermal rates significantly suppressed, speculating on a potential barrier for activation effectively enhanced by the interaction of the macroscopic degrees of freedom in the device, Han et al. [56] find excellent agreement with the predictions for thermally activated transitions using Nb/$Al_2O_3$/Nb JJs. In these experiments the junctions composing the SQUID are strongly coupled, so that the two normal-mode frequencies were very different. In such case the fast stable mode rapidly adjusts on the lower unstable one. The two junctions are thus locked on each other, and the dynamics of the system is not very different from the single-junction case, as discussed in [57]. In the experiment from [57] focussed on the TA regime, the junctions are loosely coupled, and are not reducible to one junction. Nb/Pb-In SQUIDs measured in [57] differ only by their loop inductance. The zero-voltage state of these SQUIDs is in general not unique, but can correspond instead to several metastable states. Each of these substates is associated with a given number of flux quanta trapped in the superconducting loop of the SQUIDs. The existence of this multiplicity is a direct consequence of the two-dimensional character of the dc-SQUID dynamics [57]. Results are consistent with the predictions for thermally activated transitions, in agreement with [56]. Tunneling from the zero-voltage state

of the dc SQUID based on NbN/AlN/NbN [58] and Al/$AlO_x$/Al [59] JJs has been found to be well described by the quantum mechanics. MQT in NbN-based junctions has been also observed in other experiments on single junctions [61, 62] (see also Sect. 11.3.4). Escape probability in a hysteretic dc SQUID has been also investigated in view of one-Shot Quantum Measurement [63].

A SQUID has been used to build a coupled system of one classical and one quantum mechanical degree of freedom, as described in [60]. The quantum degree of freedom can facilitate the escape of the whole system and this has been theoretically predicted as the "Münchhausen effect". The system has been implemented by shunting one of the two junctions of a dc SQUID with an additional capacitance. This can be also expressed in terms of the washboard potential shown in Fig. 11.8a that obviously also depends on the magnetic field. A crossover between quantum and classical escape processes related to the direction of escape has been detected. Under varying external magnetic flux, MQT periodically alternates with TA escape, a hallmark of the "Münchhausen effect". Depending on the magnetic field, the device shows either TA (see Fig. 11.8c) or MQT (see Fig. 11.8d), both at the same temperature [60]. A particle with strongly anisotropic mass displays either quantum mechanical or classical behavior, depending on the direction of escape. Hence, coupling a classical to a quantum mechanical degree of freedom can facilitate the escape of a particle in a 2D potential considerably compared to a purely classical system [60] (see Fig. 11.8b).

Still connected to the ability of changing the washboard potential by using the magnetic field, quantum properties of a single Josephson vortex in a Nb/$AlO_x$/Nb annular junction (schematized in Fig. 11.9a) subject to an in-plane magnetic field $H$ have been investigated [64]. By measuring the statistics of the vortex escape from a controllable pinning potential (see Fig. 11.9a), the existence of quantized levels of the vortex energy within the trapping potential well and quantum tunneling of the vortex through the pinning barrier have been demonstrated [64]. The I-V curve is shown in Fig. 11.9b. The transition from TA to MQT is observed through SCD measurements as a function of $T$ (see Fig. 11.9c) and through the temperature dependence of the standard deviation $\sigma$ for two different values of the magnetic field (see Fig. 11.9d) [64].

## 11.2 Moderately Damped Regime

There has been a growing evidence of the occurrence of a moderately damped regime (MDR) in superconducting JJs of various materials [65–75]. Keeping in mind the definition of the $Q = \omega_J RC$ parameter, a MDR is present for $1 < Q < 5$. This regime is quite distinct from the well-known case of underdamped systems ($Q > 10$) discussed up to now, and apparently quite common in junctions characterized by low $I_c$ or by larger dissipation, intrinsic of the nature of the junction. In view of a more and more relevant use of nanotechnologies in superconducting electronics and therefore of low values of $I_c$, studies on MDR are of relevance for all types of nanoscale junctions.

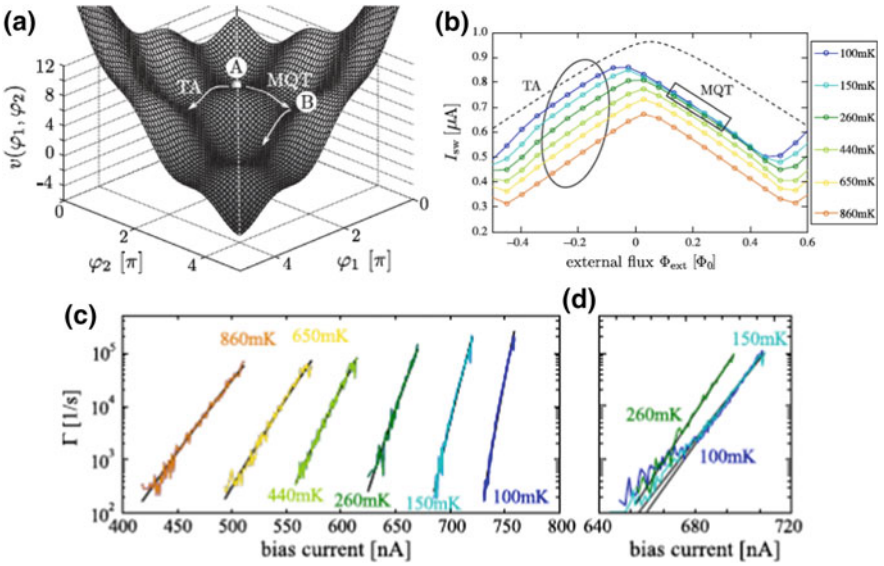


**Fig. 11.8** **a** 2D potential landscape of a dc SQUID with two identical junctions for $k = 1/\beta_L = \Phi_o/(2\pi LI_c) = 0.17$ at a normalized bias current of $i = 0.2$ and in absence of an external magnetic field. $\varphi_1$ and $\varphi_2$ refer to the the phase difference across the respective JJs, and $L$ is the loop inductance (for more details on SQUID layout and notions, see Chap. 14). **b** Temperature and flux dependence of the mean switching current. Circles indicate measured values, lines are guides to the eye. The black oval and rectangle indicate data points used for the fitting of TA and MQT rates, respectively. The dashed line is the calculated fluctuation free critical current corresponding to the state with zero magnetic flux quanta in the loop. **c** TA rates at $\Phi_{ext}/\Phi_o = -0.24$. **d** MQT rates at $\Phi_{ext}/\Phi_o = 0.24$ for the three lowest temperatures. From [60]

In the MDR regime, the phase dynamics is quite modified: following an event of escape, the particle may travel down the potential for a few wells and then may be retrapped in one of the following minima (see Fig. 11.10) [65]. A decrease of the Josephson energy $E_J$ and of the quality factor $Q$ enhances the retrapping rate $\Gamma_r$, see (11.11), causing multiple retrapping phenomena in the switching dynamics. At low bias the process of escape and retrapping may occur multiple times, generating extensive diffusion of the phase until an increase of the tilt of the potential, due to a change in the bias current, raises the velocity of the particle and the junction can switch to the running state. This is known as Phase Diffusion (PD) regime [65] (in literature it is also said underdamped phase diffusion to distinguish from phase diffusion in overdamped junctions) and has been already introduced in Chaps. 1 and 7. The significance of the analysis of phase diffusion phenomena extends to the more general problem of the motion of a Brownian particle in a periodic potential [65, 74, 76]. PD manifests itself as an unexpected collapse of switching current fluctuations with increasing $T$ due to the interplay of two counteracting consequences of thermal fluctuations [68]. On one hand, thermal fluctuations assist in premature switching into the running state and, on the other hand, help in retrapping back to

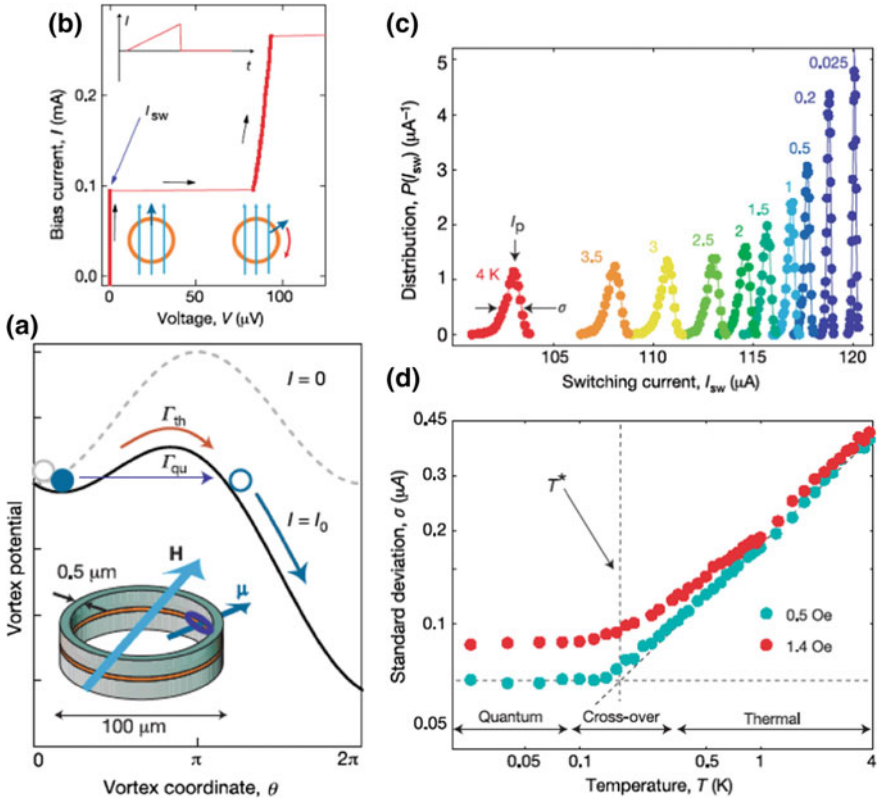


**Fig. 11.9** **a** A vortex with magnetic moment $\bar{\mu}$ trapped in an annular JJ subject to an in-plane external magnetic field $H$, shown in the inset. The resulting vortex potential at zero bias current $I$ (dashed line) and at finite bias (solid line) is plotted versus the vortex coordinate $\theta$ in the annulus. **b** I-V characteristic showing the vortex depinning from the field induced potential at a random value of bias current when ramping up the bias current at a constant rate in a saw-tooth pattern (see upper inset). **c** SCDs at magnetic field $H = 0.9$ Oe for bath temperatures $T$ between 4.0 K and 25 mK. **d** Temperature dependence of $\sigma$ for two values of field, indicating the crossover in the vortex escape process from TA to MQT. From [64]

the superconducting state [68]. In other words, temperature does not only provide energy for excitation of a system from equilibrium state but also enhances the rate of relaxation back to the equilibrium.

This phenomenon of PD shows clear fingerprints when studying the temperature dependance of the switching distributions [66–75], as shown in Fig. 11.11 [74]. Differently from the underdamped case, where the width $\sigma$ of the SCDs has a monotone temperature dependence as $\sigma \propto T^{2/3}$, in the case of moderately damped junctions the switching dynamics is modified. Below a transition temperature $T^*$ the width of the switching distributions follows the usual $\sigma \propto T^{2/3}$ and the corresponding maximum amplitudes of normalized SCDs decrease when increasing the temperature (red

curves in Fig. 11.11a), while for $T > T^*$ the characteristic collapse of $\sigma$ is observed with increasing $T$, as shown in Fig. 11.11b, and the maximum amplitudes of the SCDs increase in this temperature range (blue curves in Fig. 11.11a). If $T_{cr} < T^*$, at the lowest temperatures the transition from TA to MQT is not affected [66–70, 74].

Such a counterintuitive behavior of $\sigma$ can be explained in the following way: in presence of retrapping processes, a single escape event does not lead to the switching to the voltage state; when a larger number of fluctuation events are needed in order to induce the transition to the running state, the stochasticity in the switching process is smaller and, hence, the distributions of switching currents are sharper. This phenomenon affects also the shape of the SCDs: while in the TA regime the switching hystogram is asymmetric with the characteristic tail of the ascending side of the distribution (see Fig. 11.11c), in the PD regime the histograms are more symmetric because multiple retrapping prevents the switching at lower values of the bias current, thus causing the progressive truncation of the tail on the ascending side of the SCD, as shown in Fig. 11.11d. In Fig. 11.12, we collect data from experiments on different types of junctions, which further confirm all qualitative behavior shown in this section.

In Table 11.2 a non exhaustive list of Josephson devices that have displayed PD behavior is reported with indications on the most relevant device parameters. Exper-

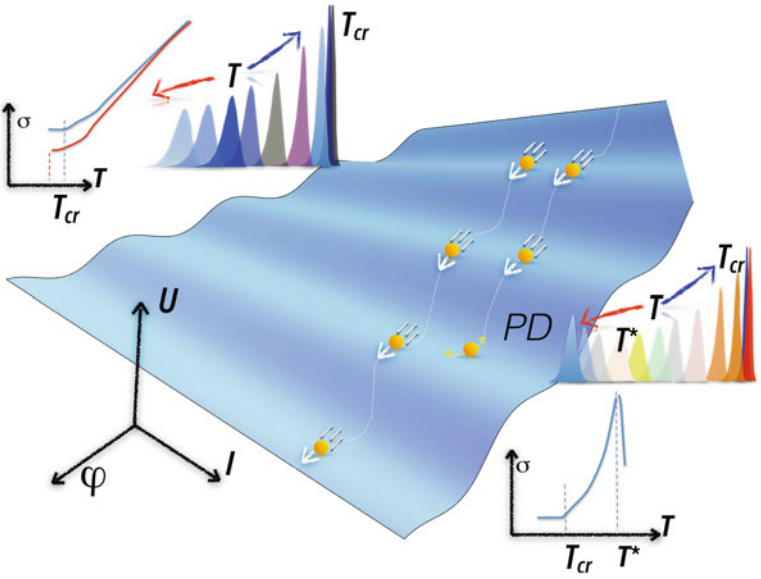


**Fig. 11.10** 3D cartoon of the washboard potential with a comparison between standard running state following TA or MQT escape and PD with phase retrapping. Phase trajectories are artificially shifted along the current axis for sake of clarity. SCDs and the corresponding widths have quite distinctive qualitative behaviors, that are shown in the two insets. While in the upper-left inset $\sigma$ has a monotonic temperature dependence above $T_{cr}$, in the lower-right inset the characteristic collapse of $\sigma$ occurs above a transition temperature $T^*$

imental results point in the same direction of PD, but their interpretation slightly differs in few assumptions, as properly pointed by Fenton and Warburton [71]. For instance Kivioja et al. [66] interpreted their results on dc-SQUIDs within the semi-classical model of Larkin and Ovchinnikov [48, 49]. Since in dc-SQUIDs there are few energy levels and the hypothesis of continuous energy spectrum is not valid, they used a model which takes into account both phase diffusion and level quantization. The transition temperature $T^*$ is expected to occur at $E_J(1-4/(\pi Q))^3/(2k_B)$ [69]. On the other hand this model, which assumes separated levels in the metastable well, is not properly valid for a single JJ since the number of energy levels is large and the separation is smaller than their width. Männik et al. [67] and Bae et al. [72] calculated the retrapping probability through Monte Carlo simulations and included frequency dependent damping. In [67] PD appears in magnetometers with much larger and unshunted junctions used for qubits readout. The authors express the net escape rate as a sum of probabilities of multiple escape-retrapping events based on thermal escape rate and retrapping probability. The probability of retrapping is considered as a time-independent quantity which is in contrast with the work of Ben-Jacob et al. [52], in which retrapping is modeled by a rate and therefore the probability is proportional to the time spent in the running state.

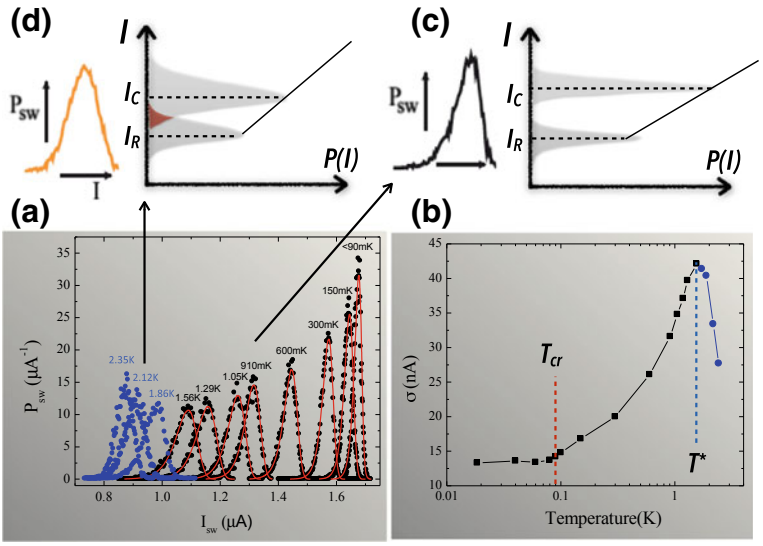


**Fig. 11.11** **a** Measurements of SCDs as a function of the temperature in the MDR. Red curves are fits of the SCDs in the TA regime while blue points are measured histograms in the PD regime. **b** Temperature dependence of the standard deviation $\sigma$ of the switching distributions. Three characteristic regimes can be distinguished: for $T < T_{cr}$ MQT, for $T_{cr} < T < T^*$ TA and for $T > T^*$ PD, respectively. **c** Asymmetric SCD in the TA regime, when thermal escape and retrapping processes do not overlap. **d** In the PD regime, distributions become more symmetric since there is a range of currents where escape and retrapping processes overlap, leading to the truncation of the tail of the SCD. From [74]

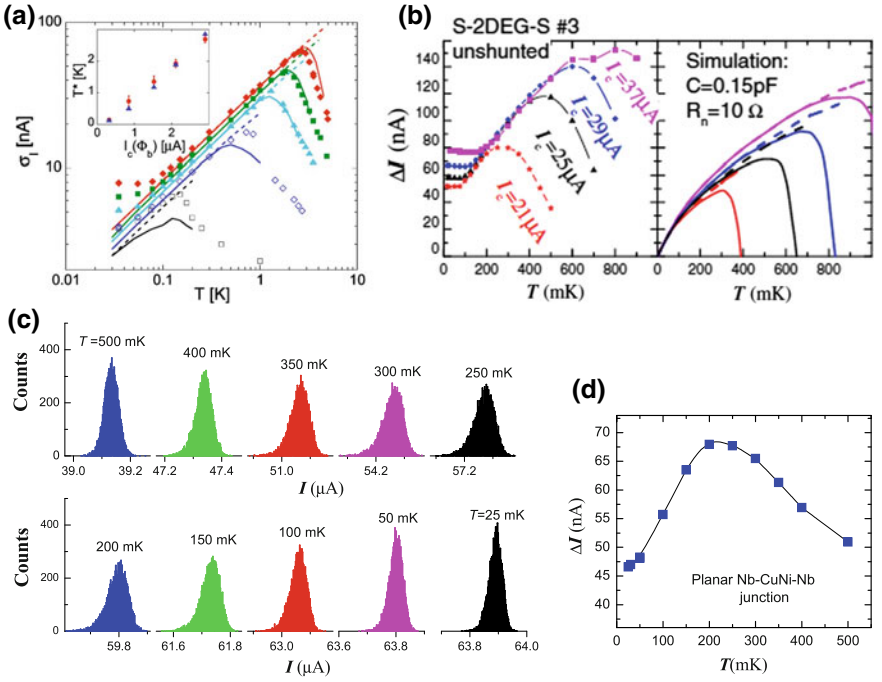


**Fig. 11.12** Moderately damped dynamics of different Josephson systems. **a** Standard deviation $\sigma$ of SCDs as a function of temperature for a dc-SQUID, fabricated using a self-aligned Nb trilayer process, for different values of the external flux bias $\Phi_b$. The potential of the SQUIDs can be well approximated by that of a single junction with an effective critical current $I_c(\Phi_b)$. The inset shows $T^*$ dependence as a function of the effective $I_c$. From [67]. **b** Temperature behavior of the width in moderately damped Nb-InAs-Nb JJs, at four magnetic fields (left panel) and numerical simulations taking into account both thermal escape and retrapping processes, right panel. From [68]. **c** Measurements of SCDs of planar ferromagnetic JJ with barrier made of CuNi. The histograms become wider with increasing $T$ up to $T = 200$ mK (lower row) but then the width starts to shrink at $T \geq 250$ mK (upper row). The corresponding $\sigma$ is shown in panel (**d**). From [70]

A comparative deep analysis on the anticorrelation between temperature and fluctuations of the switching current in moderately damped JJs is carried out in [68, 70], with measurements on ferromagnetic junctions such as Nb-CuNi-Nb (SFS) junctions, on low ohmic Nb-Pt-Nb (SNS) junctions and Nb-InAs-Nb (S-two dimensional electron gas-S) structures. This confirms how general the effect of dissipation is on all types of junctions, when falling in the appropriate windows of parameters. The work from Fenton and Warburton contains a considerable amount of Monte Carlo simulations of thermal fluctuations in moderately damped JJs with insights on multiple escape and retrapping processes, switching- and return-current distributions [71].

Longobardi et al. [74] followed arguments developed by Fenton and Warburton [71], and used the following Langevin differential equation to simulate the stochastic dynamics:

**Table 11.2** Comparison of device parameters of different Josephson systems in the moderately damped regime

| Author | Device Structure | R ($\Omega$) | $I_c$ ($\mu A$) | C ($fF$) | $Q(I=0)$ |
|---|---|---|---|---|---|
| Kivioja et al. [66] | Al/AlOx/Al dc-SQUID | 500 | 0.2 | 100 | 3.9 |
| Kivioja et al. [66] | Al/AlOx/Al JJ | 230 | 0.63 | 130 | 3.6 |
| Männik et al. [67] | Nb/AlOx/Nb dc-SQUID | 70 | 4.25 | 90 | 2.4 |
| Männik et al. [67] | Nb/AlOx/Nb dc-SQUID | 70 | 2.9 | 260 | 3.3 |
| Krasnov et al. [68] | S-2DEG-S | 10 | 37 | 200 | 1.6 |
| Krasnov et al. [68] | Bi-2212 Intrinsic JJ | 40 | 80[1] | 685 | 5.6 |
| Bae et al. [72][2] | Bi-2212 Intrinsic JJ | 62 | 1.26 | 330 | 2.2 |
| Yu et al. [73] | Nb/AlOx/Nb JJ | 1800 | 0.122 | 20 | 4.8 |
| Yu et al. [73] | Nb/AlOx/Nb JJ | 315 | 0.48 | 77 | 3.3 |
| Longobardi et al. [74] | NbN/MgO/NbN JJ | 65 | 1.91 | 300 | 2.7 |
| Longobardi et al. [77] | YBCO GB BP JJ | 84 | 1.20 | 64 | 1.30 |

[1]This is the value of the critical current at the transition temperature $T^* = 75$ K
[2]In this paper the authors estimated the fit parameters to be temperature dependent. Here we report the values at the lowest experimental temperature $T = 1.5$ K

$$\varphi_{tt} + \varphi_t/Q + i + i_N = 0 \tag{11.15}$$

Times $t$ are normalized to $1/\omega_J$; $i$ is the bias current normalized to critical current $I_c$ and $i_N$ is a Gaussian correlated thermal noise current, i.e.:

$$\langle i_N(t), i_N(t') \rangle = \sqrt{2\pi k_B T/QI_c\Phi_o}\,\delta(t-t').$$

The damping parameter $Q(\omega)$ has a frequency dependence better responding to the need of including the external shunting impedance [30, 65], as already discussed in Chap. 7. Since phase diffusion involves motion of the phase particle at the plasma frequency $\omega_J$, while the finite voltage state involves steady motion at $\omega \simeq 0$, the frequency dependent $Q(\omega)$ has lower values at higher frequencies near $\omega_J$ [65], where the characteristic resistance is mainly due to the bias circuitry [30], and higher values at zero frequency, where the intrinsic resistance of the junction dominates [65] (see also Fig. 11.18).

Simulated curves of $\sigma$ versus $T$ for different values of the magnetic field are plotted in Fig. 11.13. The magnetic field works as a knob to tune $T^*$ and provides an additional validity test for the estimate of the high frequency quality factor $Q = 2.7 \pm 0.1$ in absence of magnetic field. The fall off of $\sigma$ allows an accurate estimation of the high frequency $Q$ factor through a fitting procedure based on Monte Carlo simulations [71, 77]. This method is of general utility for all types of junctions in the MDR, where it is not always easy to quantify dissipation through standard technique based on resonant activation measurements [30]. Remarkably all parameters are consistently

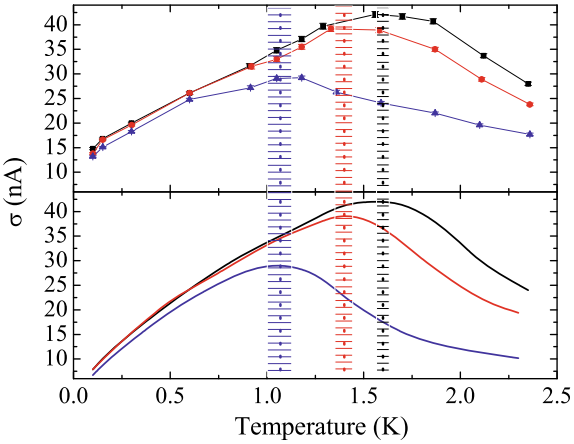


**Fig. 11.13** Top frame: temperature dependence of the standard deviation $\sigma$ of the switching distributions for $B = 0$ G (squares), $B = 3.1$ G (circles), and $B = 6.1$ G (triangles). Bottom frame: a numerical simulation of the data. Vertical dotted lines have been inserted in correspondence of the values of $T^*$ including error bars. Data and numerical simulations are in good agreement in the whole temperature range and for all magnetic fields within error bars. From [74]

calculated. From $T_{cr}$, once known the $Q$ value from the phase diffusion fitting, first $C$ and the plasma frequency $\omega_J$ are inferred, and finally the value of the shunting resistance $R$ can be determined. As in the experiments reported in [30, 31], values of $R$ range from 50 to 100 Ω [67, 68, 72, 74, 77], confirming the crucial role played by the bias circuitry. In [74], the values obtained for the junction capacitance and plasma frequency at zero bias current are $C = 0.3$ pF and $\omega_J(0) \simeq 22$ GHz, respectively.

PD manifests characteristic benchmarks also in the escape rates $\Gamma$, shown in Fig. 11.14 as a function of the ratio between the barrier height and the thermal energy [67]. The escape rates are calculated from the switching distributions using (11.6). In the thermal activation regime the distributions are asymmetric and skewed to the left, and $\Gamma$ values all fall onto the same line, as it is the case for the reported data from $T = 0.3$–$1.56$ K. Retrapping processes cause a progressive symmetrization of the switching distribution, as it can be seen from the inset in the bottom left corner of Fig. 11.14, and in the bending in the $\Gamma$ versus $u = \Delta U/k_B T$ curve. The same value of the $Q$ factor has been obtained by fitting the $\Gamma(u)$ curves, shown as dashed lines in Fig. 11.14.

The symmetrization of the switching distribution due to the interplay between escape and retrapping events can be clearly observed by plotting, as a function of temperature, the skewness of the distributions $\gamma$ that is, the ratio $m_3/\sigma^3$ where $m_3$ is the third central moment of the distribution. For the data with no external magnetic field, the plot is shown in the inset of Fig. 11.14. For the lowest temperatures $\gamma = -1$ is obtained, which is consistent with the case of switching current distributions in the quantum or thermal regime [74]. As the temperature increases the distributions become more and more symmetric as $\gamma$ tends to zero. In [74], the temperature $T^*$

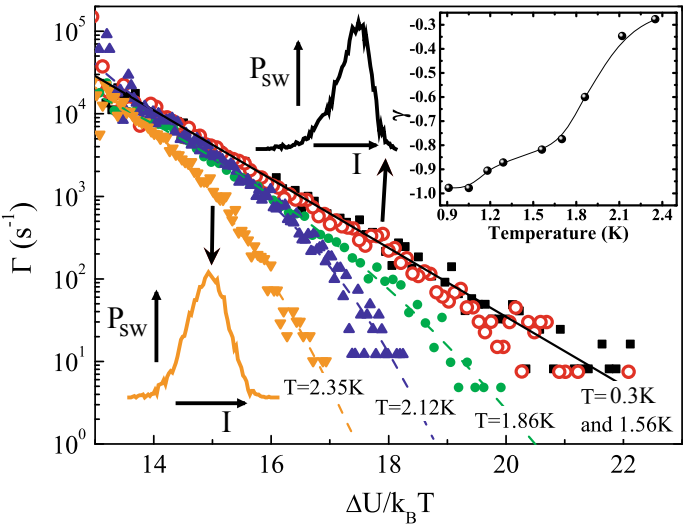


**Fig. 11.14** Escape rates (symbols) as a function of the barrier height at zero magnetic field, for temperatures near $T^*$, and numerical simulations (dashed lines). Below $T^*$ the fit has been calculated using Kramers formula for thermal activation (solid line). The inset shows the experimental value of the skewness of the switching distribution. From [74]

at which the derivative of $\sigma(T)$ changes sign is equal to $1.62 \pm 0.3$ K, while the skewness starts increasing already at about 1.2 K, which is an indication that the onset of retrapping phenomena occurs well below $T^*$ [71].

## 11.3 Thermal Activation, Macroscopic Quantum Tunneling and Phase Diffusion in Unconventional Josephson Junctions

Studies on phase dynamics and macroscopic quantum phenomena have been in the last few years extended to novel types of structures and materials. We will refer as novel types of junctions, those composed of novel materials, or devices scaled to the nano-size or based on novel design concepts other than the classical trilayer structure, as intrinsic junctions in HTS or junctions using nanowires as barriers. SCD measurements have turned to be standard tools to investigate the phase dynamics also in unconventional and hybrid systems, to give new arguments on dissipation and to define conditions for which MQT can be observed.

### 11.3.1 HTS Josephson Junctions

HTS JJs are an example of unconventional systems, because of the d-wave order parameter (OP) symmetry and of the presence of low energy quasi-particles (see Chaps. 8 and 9), which are expected to induce high levels of dissipation and as a consequence to spoil macroscopic quantum coherence [78]. Low energy quasi-particles have represented since the very beginning a strong argument against the occurrence of macroscopic quantum effects in these materials. Quantum tunneling of the phase leads to fluctuating voltage across the JJ, which excites the low energy quasi-particles specific for d-wave junctions, causing decoherence. Contributions to dissipation due to different transport processes, such as channels due to nodal quasi-particles, midgap states, or their combination, have been theoretically identified and distinguished [78–80].

The first experiment has been realized on $CeO_2$ based biepitaxial (BP) YBCO grain boundary (GB) junctions (see Sect. 8.3.2). These junctions met some of main requirements necessary for SCD experiment, as an apparently underdamped behavior with hysteresis up to 90%, with $I_c$ values of a few $\mu$A. In addition the BP technique gave the possibility to select opportune misorientation angle and thus to tune the population of low energy quasiparticles and their possible deleterious effect on macroscopic quantum behavior. The tilt configuration (angle $\theta = 0°$) has been selected in order to have the lobe to node configuration, which maximizes d-wave induced effects and allows to explore damping also due to low energy quasi-particles [81].

Figure 11.15 shows a set of SCDs as a function of the temperature for a YBCO GB BP JJ [81]. The dependence of the distribution width $\sigma$ on temperature is reported in the inset (a) of Fig. 11.15. The measured $\sigma$ saturates below 50 mK, indicating a crossover from the thermal to the MQT regime. To rule out the possibility that the saturation of $\sigma$ is due to any spurious noise or heating in the measurement setup, the SCDs were measured for a reduced critical current by applying an external magnetic field $B = 2$ mT ($I_c = 0.78$ μA from the original $I_c = 1.40$ μA at zero field). The width $\sigma$ for $B = 2$ mT and the data for $B = 0$ mT are shown in the inset (b) of Fig. 11.15. The data in the presence of a magnetic field clearly show a smaller width $\sigma$, which does not saturate down to the base temperature [81], in agreement with the outcomes of the experiments reported in [29, 30].

Additional solidity to the conclusions of the experiment is given by a self-consistent estimation of all junction parameters with a plasma frequency $\omega_J(0)/2\pi \simeq 7.8$ GHz [81] and by later measurements in presence of microwaves [82], where energy level quantization has been proved. Values of $R \simeq 100\ \Omega$, $C_J \sim 0.22$ pF (where $C_J$ is the capacitance of the junction itself to distinguish from other contributions, primarily in this case the stray capacitance of the electrodes caused by the large dielectric constant of the substrate) and $Q \sim 40$ can be obtained from the measurements [81–84]. $C$-axis tilt is mostly responsible for low barrier transparency and leads to the presence of a significant kinetic inductance in the modeling of YBCO JJ. In these junctions, the presence of a kinetic inductance and of a stray capacitance determines the main difference in the washboard potential, making the system behav-

ior depending on two degrees of freedom [82–84]. The YBCO JJ is coupled to this LC-circuit and the potential becomes two-dimensional. Inductance of the LC circuit and stray capacitance can be also estimated [84]. The observation of MQT even for junctions with a lobe of the OP facing a node demonstrates that the quality factor $Q$ of HTS GB JJs is however high enough to observe macroscopic quantum behaviors and that low energy quasi-particles in d-wave JJs are less harmful and dissipative than expected [82].

In later studies, junction parameters have been finely tuned to explore phase dynamics in the MDR, in poorly explored regimes [77, 85, 86]. MQT, TA and PD, along with the transitions from one to another regime have been investigated as a function of $Q$ and $E_J$. $T_{cr}$ from TA to MQT has been found within the temperature range from 50 to 140 mK, with $\omega_J$ of the order of 10 GHz and a $Q$ factor ranging from 40 in the underdamped regime [82, 84] to about 1 in the MDR [77, 85]. Capacitance values range from 60 fF in JJs based on $(La_{0.3}Sr_{0.7})(Al_{0.65}Ta_{0.35})O_3$ (LSAT) substrates [87] to about 1 pF in $SrTiO_3$ (STO) based JJs [81, 88, 89]. In general, values of specific capacitance of off-axis BP junctions on STO substrates are about $5 \times 10^{-4}$ F cm$^{-2}$, one order of magnitude larger than those found for LSAT

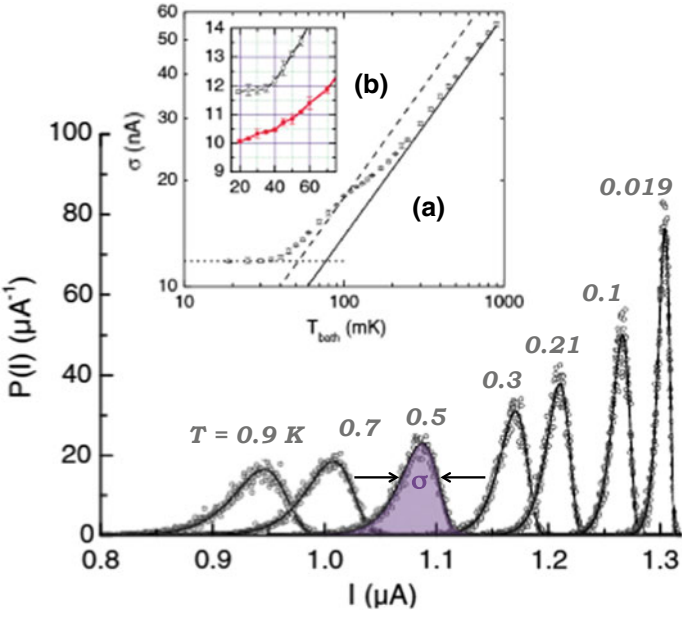


**Fig. 11.15** SCDs for a BP YBCO junction at $B = 0$ T for different bath temperatures $T_{bath}$. In the inset (**a**) the corresponding temperature dependence of the width $\sigma$ is reported in log-log scale. In the upper small inset (**b**), $\sigma$ is reported for two different magnetic fields at $B = 0$ T (open circles) and at $B = 2$ mT (closed symbols), demonstrating that flattening of $\sigma$ indicates macroscopic quantum tunneling. From [81]

based junctions [88] (see also Chap. 8), thus demonstrating some tuning on shunting parasitic capacitance.

MQT has also been calculated for d-wave $c$-axis tilt JJs and for traditional GBs through the effective action starting from the microscopic Hamiltonian, without any phenomenological assumption. The MQT is strongly suppressed for zero twist angle, when compared with the finite twist angle case [80]. In the case of $d_0 - d_0$ junctions, the dissipation is the same super-ohmic type as in the case of the $c$-axis junctions [80].

#### 11.3.1.1 Effect of the Second Harmonic Component in SCDs

HTS JJs also raised questions about the possible effects due to a second harmonic component [90, 91] in the $I_s(\varphi)$. These arguments have also been relevant for ferromagnetic junctions [62, 92] and experimental data will be presented in Sect. 11.3.4. The considerations developed in Sect. 11.1.1 can be extended to a more complicated "tilted washboard" potential $U$, where effects related to the presence of a second harmonic (see Fig. 1.12c) are taken into account, and $I_c = I_1 \max_\varphi \{\sin\varphi - g \sin 2\varphi\}$, where $I_1$ is the first harmonic current and $g = I_2/I_1$ defines the strength of the second harmonic. For large values of the second harmonic component, the potential obviously has the shape of a double well profile [62, 82, 91, 92].

For $g < 0.5$ the potential is single welled, while for $g > 0.5$ the potential has the shape of a double well [90–92]. Depending on the temperature, damping parameter and strength of the second harmonic component $g$, the phase can escape into the running state from the lower lying well of the tilted "double-welled" washboard potential, or may escape from both wells, resulting in two different critical currents. In the experiment reported in [81], the analysis was restricted to $g < 2$.

For normalized bias current $i$ close to one, the expression for the plasma frequency is $\omega_J(i, g) = c(g)^{-1/2} \left(2\pi I_c/\phi_0 C\right)^{1/2} \left(1 - i^2\right)^{1/4}$, with the renormalization factor $c(g) = \left[\left(0.5 + 3/\left(2\sqrt{1 + 32g^2}\right)\right)/2\right]^{1/2}$.

The escape rates have a minor quantitative correction expressed through the $c(g)$ parameter:

$$\Gamma_t(i, g) = a_t \frac{\omega_J(i, g)}{2\pi} \exp\left(-\frac{\Delta U(i, g)}{k_B T}\right), \tag{11.16}$$

where $\Delta U(i, g) = c(g)\left(E_J 4\sqrt{2}/3\right)(1 - i)^{3/2}$ is the barrier height for $i$ close to one. The escape rate dominated by MQT at low enough temperature for $Q > 1$ and $i$ close to one will be expressed as:

$$\Gamma_q(i, g) = a_q \frac{\omega_J(i, g)}{2\pi} \exp\left[-7.2 \frac{\Delta U(i, g)}{\hbar \omega_J(i, g)}\left(1 + \frac{0.87}{Q}\right)\right]. \tag{11.17}$$

For a pure $\sin\varphi$ $I_s(\varphi)$, the typical expressions for $\omega_J$, $\Delta U$, $\Gamma_{q,t}$ are recovered by setting $g = 0$. The second harmonic component reduces the barrier height $\Delta U$ compared to the case of a pure $\sin\varphi$ relation for a fixed critical current $I_c$, and increases the plasma frequency $\omega_J$ at bias currents $i$ close to one. Consequently, the escape rates in the thermal and quantum regimes will be larger for $g > 0$ than for $g = 0$, as a consequence of (11.16) and (11.17).

#### 11.3.1.2 SCDs in Intrinsic Junctions

Another class of experiments on the study of phase dynamics has been realized on $Bi_2Sr_2CaCu_2O_8$ intrinsic Josephson junctions (IJJs) [93, 94]. Interest has been directed to increase the crossover temperature $T_{cr}$ and to clarify the nature of IJJs. $T_{cr}$ has been reported to be about 800 mK in [94]. By using microwave spectroscopy, the unique uniform array structure of IJJ stacks have been considered responsible for a significant enhancement of the tunneling rate. This enhancement adds a factor of approximately $N^2$ to the quantum escape rate of a single JJ, also resulting in a significant increase of $T_{cr}$, where $N$ is the number of the junctions in the stack. According to [94], this effect can be caused by large quantum fluctuations due to interactions among the $N$ junctions.

In [68], a systematic analysis on PD in $Bi_2Sr_2CaCu_2O_8$ IJJs has been discussed, following previous investigations reported in [95, 96]. In [72], multiple-retrapping processes in a hysteretic $Bi_2Sr_2CaCu_2O_8$ IJJ with a high tunneling resistance govern the switching from a resistive state in the phase diffusion branch into the quasiparticle tunneling state. The frequency-dependent junction quality factor determines the observed temperature dependence of the switching current distributions and the switching rates. More details will be discussed in Chap. 10.

### *11.3.2 In the 'Far' Low Critical Current Regime in LTS and HTS JJs*

In Sect. 11.2, the moderately damped regime has been widely discussed in terms of the temperature behavior of the SCDs and in most of the mentioned experiments, the condition $E_J \gg k_B T$ was satisfied. A further reduction of $I_c$ leads the junction into another regime, where the Josephson energy becomes comparable with the thermal energy, and effects due to the phase diffusion can be visible also in the I-V characteristics [65, 97–99], as previously mentioned in Chap. 7.

This regime where $E_J$ is further reduced has been studied in submicron Nb/$AlO_x$/Nb [73], Al/$AlO_x$/Al [75] and YBCO BP [77, 89] JJs. In [73] an anomalous $\sigma(T)$ dependence with a negative $d\sigma/dT$ is reported over the entire temperature range. This regime can be achieved by engineering junctions with lower $I_c$ and $C$, such that the ratio $I_c/C$, which regulates the quantum crossover temperature $T_{cr}$, is

constant and the transition temperature $T^*$, which depends only on $I_c$, is lower or comparable to $T_{cr}$. In this specific experiment, the submicron junction of nominal cross section of $0.52\,\mu m^2$ had a reference junction of cross section of $1.61\,\mu m^2$. The estimated junction parameters for the submicron sample are: $I_c = 122$ nA, $C = 19.6$ fF, $R_n = 15\,k\Omega$, $R = 1800\,\Omega$, $T_{cr} = 140$ mK, $T^* < 25$ mK, while for the micron size one: $I_c = 480$ nA, $C = 77$ fF, $R_n = 3.84\,k\Omega$, $R = 315\,\Omega$, $T_{cr} = 125$ mK, $T^* \approx 450$ mK. While for the micron size sample a conventional temperature dependence of $\sigma$ for moderately damped junctions has been observed, see Fig. 11.16c, for the submicron sample, for which $T_{cr} < T^*$, $\sigma$ showed a monotonic increasing behavior when decreasing $T$ with a characteristic change of slope at about $T_{cr}$, see Fig. 11.16b. Experimental data for the submicron junction are consistent with a two-step transition model used to describe the switching process, in which the thermal or quantum escape rate out of the potential well, $\Gamma_1$ in Fig. 11.16d, and the transition rate from phase diffusion to the running state, $\Gamma_2$ in Fig. 11.16d, are considered [73]. The much slower process plays the major role in determining $P(I)$. Yu et al. [73] discuss the difference between classical PD and quantum PD in terms of the temperature dependence of the

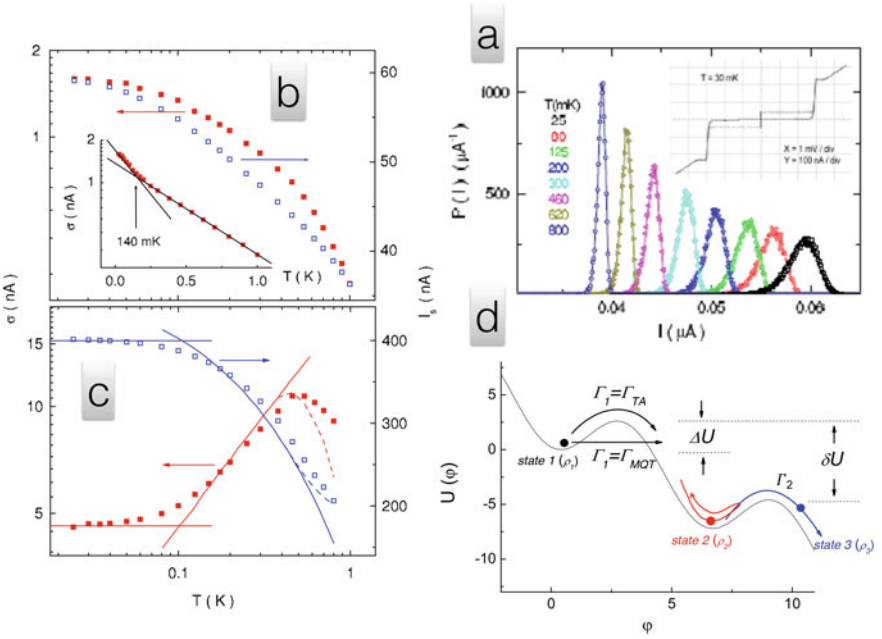


**Fig. 11.16** **a** Measurements of probability density of switching $P(I)$ at different temperatures on a submicron Nb/$AlO_x$/Nb JJ. The inset shows the I-V characteristic at 30 mK. **b** Width $\sigma$ (red squares) and mean $I_s$ (open blue squares) of experimental $P(I)$ of the submicron junction. The inset shows the temperature behavior of $\sigma$ in semilogarithmic scale and highlights the change of slope at 140 mK. **c** $\sigma$ and $I_s$ for the micron size junction along with calculations from TA and MQT theories (solid lines) and Monte Carlo simulations in the PD regime (dashed lines). d) Motion of the phase particle in the trapped (state 1), diffusion (state 2) and running (state 3) with occupation probability $\rho_n$ in the tilted washboard potential. From [73]

transition rate $\Gamma_2$. Above $T_{cr}$, $\Gamma_2$ obeys the Arrhenius classical law, while it displays a much weaker $1/T$ dependence below $T_{cr}$. Building on an analogy with the classical PD observed by Vion et al. for an overdamped system [97], Yu et al. argue that the barrier appears smaller due to the motion of the diffusive particle, and that in the thermal regime a dissipation-barrier description also holds for underdamped junctions.

In [75], Al JJs have shown similar anomalous $\sigma(T)$ dependence with a negative $d\sigma/dT$ observed over the entire temperature range. With the constraint of being in the condition where it is not possible to further lower $I_c$ in Al JJs, the only possible solution to avoid the underdamped phase diffusion regime and maintain TA process at higher temperatures was offered by including a large shunt capacitance, that was added through a sophisticated atomic-layer deposition fabrication step [75]. By increasing $C$, both the ratio $I_c/C$ and $T_{cr}$ decrease and the TA regime occurs in a wide temperature range, thus confirming the role of the capacitance in the PD phenomena [75].

For YBCO BP junctions engineered on LSAT substrates [87], a direct transition from PD regime to MQT has been demonstrated [77]. These junctions are characterized by higher $I_cR_N$ values and by specific capacitances one order of magnitude lower than those measured on STO-based devices [81, 88, 89]. Since LSAT substrates have a lower dielectric constant with respect to STO substrates, this structure allows to isolate GB contribution from stray capacitance, and tends to favor the MDR [87] (see also Chap. 8). The experiment has been designed to meet the condition $T^* < T_{cr}$ taking advantage of the characteristics of these types of junctions. Measurements of SCDs are reported in a temperature range from 20 mK to 2.2 K in Fig. 11.17a, along with the $\sigma$ dependence in Fig. 11.17b. Two distinct regimes can be distinguished at a crossover temperature indicated by $T_x$ in Fig. 11.17b. Below $T_x$ the widths of the SCDs show no significative variation. This is a typical signature of a quantum activation regime. Above $T_x$ the negative temperature derivative of $\sigma$ is consistent with a diffusive motion due to multiple retrapping processes in the potential wells. This regime has been fitted using Monte Carlo simulations [71] with a damping factor $Q = 1.3$.

The contiguity between quantum escape ($T < T_x$) and phase diffusion ($T > T_x$) leads to MQT phenomena characterized by low $Q$ values and not necessarily to quantum phase diffusion. This phenomenology is quite distinct from all previous studies [65–68, 71, 72, 77], where in the transition to quantum activation, retrapping processes decay faster than thermal escape, and from the work of Yu et al. [73], where the occurrence of a quantum activated phase diffusion has been claimed.

In Fig. 11.17c simulated temperature behavior of $\sigma$ is reported for different values of the $Q$ damping parameter ranging from 1.2 to 5. For each of these curves $T^*$ approximately indicates the transition temperature from thermal activation to the diffusive regime. $Q$ tunes $T^*$ as shown in the inset of Fig. 11.17c and modifies the slope of the $\sigma(T)$ fall-off at higher temperatures. The capability to numerically reproduce this region makes it possible to estimate $Q$ with high precision. In [77], $Q = 1.30 \pm 0.05$ closely fits the data and determines a $T^*$ value not larger than 100 mK. The section below $T^*$ reproduces the expected $T^{2/3}$ dependence for a thermally activated regime (solid line) as an additional test of consistency. In Fig. 11.17c

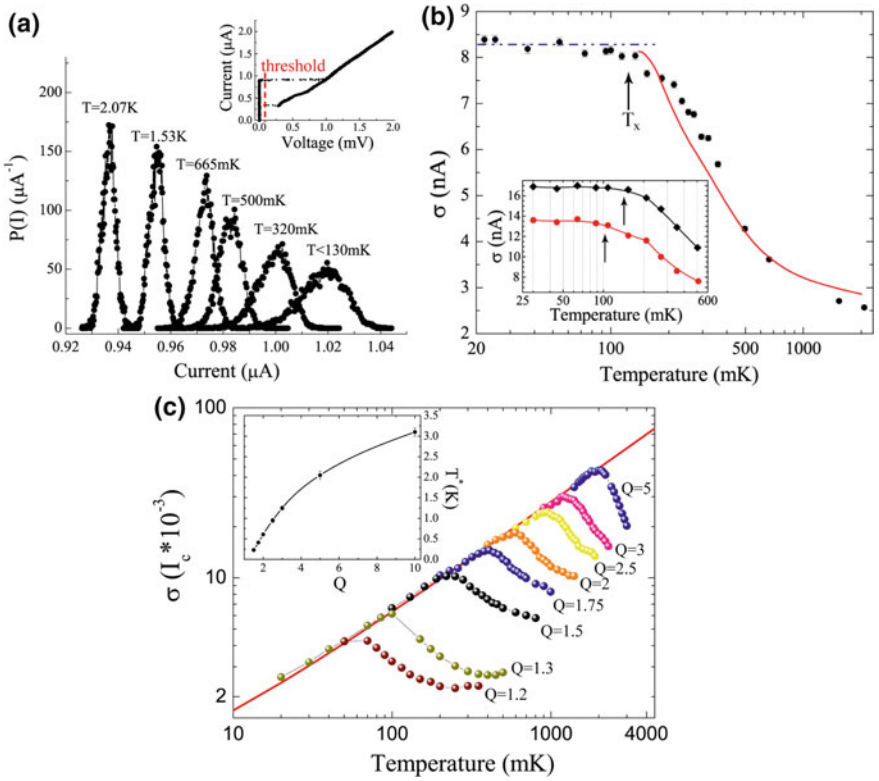


**Fig. 11.17** **a** Measured SCDs at different bath temperatures, for sample A. The inset shows the I-V characteristic of the junction measured at 30 mK. The reference value for the threshold detector is also displayed. **b** Temperature dependence of the standard deviation $\sigma$ of the switching distributions for sample A. The dash-dotted line marks the temperature-independent SCD widths in the quantum tunneling regime, the red solid line is the result of simulations in the diffusive regime with a damping parameter $Q = 1.3$. The inset shows temperature dependent data for sample B acquired at two different values of the applied magnetic field. **c** Simulated temperature behavior of the width of the switching histograms for several values of the $Q$ damping parameter. The red solid line is the expected $T^{2/3}$ dependence for a thermally activated regime. In the inset, the dependence of the transition temperature $T^*$ on the damping parameter is reported. From [77]

the MQT section is missing. It would attach below $T_{cr}$ to each of the curves with its characteristic saturation in $\sigma$, as shown in Fig. 11.17b in fitting the experimental data.

In analogy to what commonly done to prove MQT in underdamped junctions [30], the magnetic field has been used to tune in situ the junction parameters and $T_x = T_{cr}$ to unambiguously prove MQT as source of the saturation of $\sigma$ below $T_{cr}$. In the inset of Fig. 11.17b we report the temperature dependence of $\sigma$ measured for a different junction B at two values of magnetic field of 0 and 12 G respectively. $H =$ 12 G lowers the critical current $I_c$ reducing at the same time the quantum crossover

temperature. The estimated junction parameters for the investigated samples are: junction A $I_c = 1.2\,\mu$A, $C = 64$ fF, $R = 84\ \Omega$, $Q = 1.3$, $T_{cr} = 135$ mK, junction B $I_c = 1.79\ \mu$A, $C = 74$ fF, $R = 64\ \Omega$, $Q = 1.28$, $T_{cr} = 144$ mK.

In our attempt of a systematic description of SCD measurements and their correlation with the physics of the junction, we finally consider the case where $E_J$ is not anymore much larger than $k_BT$ and $E_c$. As discussed in Sect. 7.6.2, in small junctions with low values of $E_J$ a measurable resistive voltage in the nominally zero-resistance state below $I_c$ has been observed, along with a finite hysteresis in the I-V characteristic (see Fig. 7.2f). This has well accepted explanation, and I-V curves can be accurately reproduced through Monte Carlo simulations over a wide temperature range [65]. The occurrence of phase diffusion effects both in the I-V curves and in the SCD histograms has been found in a couple of experiments [89, 97, 98]. For the small-capacitance low-critical-current Al/$AlO_x$/Al junctions described in [97, 98], the thermal activation process follows a generalized Arrhenius law involving dissipation directly in its exponent. This escape over a dissipation barrier has been computed exactly for a junction connected to an $RC$ impedance providing large damping, thus the main contribution to the damping of the devices comes from the external impedance, and the junction intrinsic resistance plays no significant role. When $R$ increases, the width of switching histograms decreases, a direct consequence of the scaling of the dissipation barrier with the $RC$ time constant of the impedance. The effect of temperature is twofold. It modifies the dependence of the dissipation barrier on bias current as well as producing the fluctuations driving the system above this barrier. The current dependence of the voltage in the diffusion state prior to switching has been found to be directly related to the shape of the dissipation barrier.

In [89], a frequency-dependent damping model [65] has been used to fit experimental I-V curves of submicron YBCO BP JJs for the following values of $E_J = 270$ $\mu$eV ($I_c = 130$ nA, $J_c = 65$ A/cm$^2$) and $E_c = 45$ $\mu$eV. The switching behavior of a JJ is a high frequency phenomenon and its study in the MDR, as shown above, is commonly successfully carried out by using a single-$Q$ model to fit the experimental SCD histograms. Such a procedure works well when the condition $E_J \gg k_BT$ is satisfied and the quality factor is larger than 1. Since in [89] these two conditions were no longer satisfied, in order to consider the frequency-dependent damping a two-$Q$ model introduced by Kautz and Martinis [65] and qualitatively sketched in Fig. 11.18d, has been used, resulting in a modified Langevin equation solved through Monte Carlo simulations. The values of $Q_0 = 5$ (low frequency) and $Q_1 = 0.5$ (high frequency) well fit both the I-V curves and the SCDs [89] (as reported in Fig. 11.18c). These values are consistent with a capacitance per unit area of $1.5 \times 10^{-6}$ F cm$^{-2}$ and an effective low voltage resistance $R_o$ of about 500 $\Omega$.

Further reduction of $I_c = 35$ nA and thus of $J_c = 5$ A/cm$^2$ [89] leads the junction to a regime where the delocalization of the phase is relevant and where phenomena of quantum diffusion may play a crucial role [97, 99–105], as anticipated in Sect. 7.6.2.

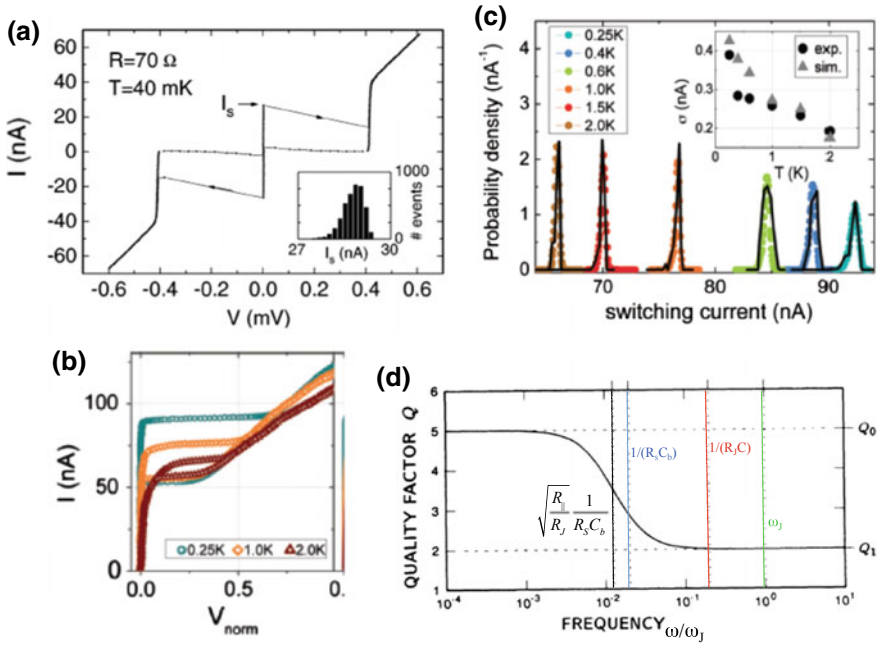


**Fig. 11.18** **a** I-V characteristic of a submicron Al/$AlO_x$/Al JJ with switching current of about 30 nA. The inset shows the switching distribution measured at 40 mK. From [97]. **b** I-V characteristics measured on a submicron YBCO GB BP JJ at $T = 0.25$, 1.0, and 2.0 K, which display the presence at the same time of the phase diffusion rounding at small voltage values and hysteresis. In panel **c** the corresponding SCDs (points) are shown and compared with simulated (black solid lines) histograms based on a frequency dependent damping model. The inset shows the behavior of the simulated (triangles) and experimental (dots) histogram width as a function of the temperature. From [89]. The model is based on the frequency dependence of the quality factor sketched in panel (**d**): a two Q-model with high frequency overdamped dynamics and low frequency underdamped behavior provides phase diffusion rounding and hysteresis in the I-V characteristics. Adapted from [65]

### *11.3.3 Phase Dynamics Diagram: Influence of Dissipation*

The progressive reduction of $Q$ moves the junctions to the MDR, as widely discussed above. The various operation regimes for a JJ have been condensed in a phase diagram by Kivioja et al. [66], who have shown that, by spanning the $(E_J, k_BT)$ parameter space, the MQT, TA and PD regimes can be identified, see Fig. 11.19a. The transitions between the various regimes can be also expressed as a function of $Q$ in the $(Q, k_BT/E_J)$ diagram obtained by numerical simulations, as reported by Longobardi et al. [77] and shown in Fig. 11.19b. The transition curve between the phase diffusion regime and the running state following thermal [66–68, 73, 74] or quantum activation [77] has been determined numerically by varying the damping factor $Q$ as a function of the ratio between the thermal energy $k_BT$ and the Josephson

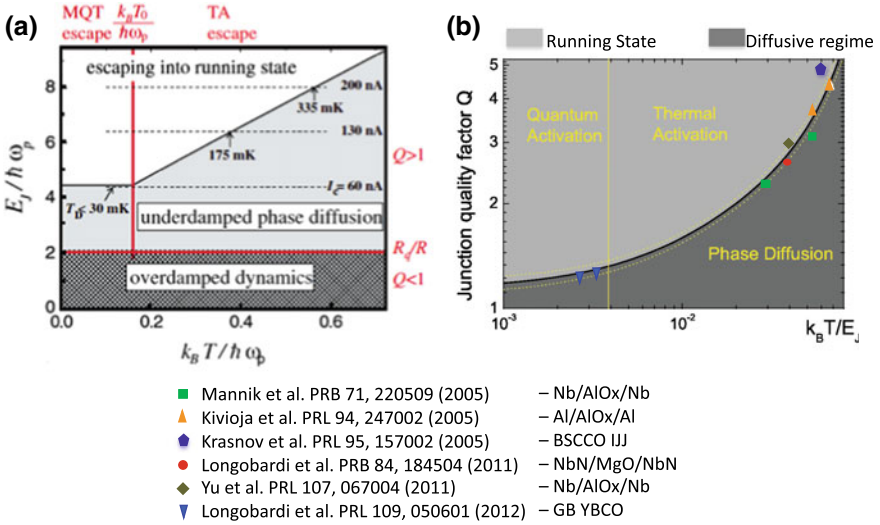


**Fig. 11.19** **a** Phase diagram of the various operation regimes of a JJ with relatively low values of $E_J$. Both $E_J$ and $k_BT$ are normalized by $\hbar\omega_p$, being $\omega_p$ the plasma frequency in [66]. In the phase diagram the regimes of quantum and thermal escape, phase diffusion and overdamped dynamics are separated by red and black solid lines. From [66]. **b** $(Q, k_BT/E_J)$ parameter space showing the various regimes. The transition curve between the PD regime and the running state has been extrapolated through Monte Carlo simulations [77], the sideband curves mark the uncertainty in calculations. This transition scales with the ratio $E_J/k_BT$ and with the damping factor $Q$, making the curve in the phase diagram universal and sample independent. The points refer to various works reported in literature [66–68, 73, 74, 77], as indicated in the legend. The yellow dashed separation line between quantum and thermal activation is peculiar of the specific sample reported in [77]. Adapted from [77]

energy $E_J$. Therefore, the result of the calculation is a universal curve which is based on the fundamental scaling energies of the JJ. The universal character of the phase diagram is demonstrated also by the good agreement with the transition points of various works reported in literature on different types of junctions, making the phase diagram an operative guide to classify all types of behaviors and a reference for phase dynamics of novel types of junctions.

At the end of this section we present a short list of significant signatures, which classify the phase dynamics of a junction and its coupling to the environment, and condense the fingerprints reported in this chapter to distinguish MDR from the underdamped regime:

1. dependence of the standard deviation $\sigma$ of the SCDs on the temperature;
2. asymmetry of the distribution measured by the skewness $\gamma$ as a function of the temperature;
3. shape of the escape rates $\Gamma$ as a function of the ratio between the barrier height $\Delta U$ and the thermal energy $k_BT$;
4. measurements reported in points 1–3 as a function of magnetic field;

5. all junction and characteristic "phase dynamics" parameters need to be estimated and to be self-consistent.

### *11.3.4 Ferromagnetic Junctions*

The interfacial coupling of two materials with different ordered phases, such as a superconductor (S) and a ferromagnet (F), is driving new fundamental physics and innovative applications. Examples are: the possibility to switch the ground state of a Josephson junction from a 0 to a $\pi$ phase state, the existence of JJs having a doubly degenerate ground state with an average Josephson phase $\psi = \pm\varphi$ (the so called $\varphi$ JJs), the possibility to carry spin-triplet supercurrent in the presence of certain types of magnetic inhomogeneity, the presence of a magnetic hysteresis for the critical current $I_c$ and therefore for the Josephson energy $E_J$. As a consequence, ferromagnetic JJs are particularly interesting for their potential applications as switching elements in cryogenic memories, bi-stable states in quantum computation and circuit elements in superconducting spintronics . Extensive reviews of the main concepts and results can be found in [106–109, 122]. Although the static properties of ferromagnetic JJs have been extensively studied, the phase dynamics of these junctions is still to be explored.

Ferromagnetic junctions can be composed by pure metallic ferromagnetic layers (SFS), by an insulating barrier and a ferromagnetic metallic layer (SIFS), and by a ferromagnetic-insulator barrier (SI$_F$S). The study of the switching dynamics reflects the different properties of the barriers as discussed in the following subsections.

#### 11.3.4.1 SI$_F$S Josephson Junctions

Underdamped dynamics, as usually observed in standard tunnel JJs, has been reported recently in NbN/GdN/NbN junctions, where GdN is an I$_F$ barrier [62]. These JJs are spin filter junctions, by changing the thickness of the GdN barrier it is possible to change their magnetic properties and hence the spin filter efficiency (SFE) [110–112]. Below about 35 K, the onset of ferromagnetism in GdN induces the spin-dependent splitting of the band structure, causing a spin polarization in the incoming charge current, because spin-up and spin-down electrons experience different effective barrier heights, and one channel is partially suppressed. The SFE is therefore defined as the unbalance between the conductivities of spin-up and spin-down electrons [110–112].

The presence of an I$_F$ barrier provides high values of the $I_cR_n$ product, up to a few mV, and hysteresis amplitude in the I-V curves larger than 90%. In these junctions, a clear transition from thermal to quantum regime at a crossover temperature of about 100 mK at zero magnetic field has been observed [62]. MQT has been observed in junctions characterized by high values of SFE, of about 90%, that corresponds to barrier thickness of about 3 nm. For the measured devices, the junction area is about

$7\,\mu\text{m} \times 7\,\mu\text{m} \simeq 50\,\mu\text{m}^2$. The values of $I_c$, $E_J$ and $I_cR_n$ are about 30 μA, 60 meV and 0.1 mV respectively.

The temperature behavior of the SCDs is typical of underdamped JJs and the standard deviation $\sigma$ increases with temperature as expected. The dependence of the standard deviation $\sigma$ on temperature is reported in Fig. 11.20a (right axis), along with the temperature behavior of the mean value of the SCDs, indicated in the figure as $I_{mean}$, below 0.5 K (left axis). When decreasing the temperature, $I_{mean}$ increases while $\sigma$ decreases and both saturate at a crossover temperature of about 100 mK. Below this crossover the histograms overlap and the escape process is no longer regulated by thermal fluctuations, indicating the transition to the MQT regime [62]. A further confirmation of the observation of MQT comes from measurements of SCDs in presence of an external magnetic field [62]. The behavior of $\sigma(T)$ at $H =$ 1.1 mT is shown in Fig. 11.20b. At this value of the magnetic field, which reduces $I_c$ to half of the value measured at zero field, lower values of $\sigma$ have been measured and $T_{cr}$ is reduced by a factor $\sqrt{2}$, down to about 70 mK, in agreement with the general MQT theory presented above. In both cases of 0 mT and 1.1 mT, $T_{cr}$ has been determined by the intersection of the $T^{2/3}$ curve and the mean value of $\sigma$ in the MQT regime [62]. The standard procedure on the fitting of SCDs provides the estimate of $I_c$ in absence of fluctuations: $I_c = 30.41 \pm 0.05\,\mu\text{A}$. Quite accurate values of the capacitance and of the plasma frequency can be determined from the crossover temperature $T_{cr}$ and from $I_c$, thus obtaining $C = 4.5 \pm 0.9$ pF and $\omega_J \approx 14$ GHz. These measurements represent the first demonstration of macroscopic quantum phenomena in ferromagnetic JJs and give promise for the application of spin filter devices as active elements in quantum hybrid circuits [113].

Recently, JJs with multiple F layer barriers have been theoretically and experimentally studied in connection to unconventional triplet superconductivity with equal-spin Cooper pairs, that can be artificially generated in these structures [106–109]. It has also been predicted that, in JJs with asymmetric spin-active interfaces, the current-phase relation $I_s(\varphi)$ could be dominated by the second harmonic component, as a consequence of the coherent transport of two triplet pairs [114, 115]. Therefore, for junctions with ferromagnetic barriers, the issues on the presence of the second harmonic, which has in the magnetic dependence of $I_c$ a crucial reference [92], are of relevance.

Strong evidence of a pure second harmonic $I_s(\varphi)$ in spin filter JJs has been reported in the work by Pal et al. [111]. In terms of the washboard potential, a second harmonic component in the $I_s(\varphi)$ may result in the appearance of a double well, as shown in Fig. 11.20c and previously discussed in Sect. 11.3.1.1. Depending on the junction parameters, for a double-well potential two critical currents could be observed, which means that the escape process may result in the observation of bimodal switching distributions. Numerical simulations of the phase dynamics as a function of the damping parameter $Q$, of the $g = I_2/I_1$ factor introduced in Sect. 11.3.1.1 and of the temperature $T$ give the conditions for which the escape from a double well potential results in a single mode or in a bimodal distribution [62]. The study of the retrapping process is crucial in order to distinguish in which conditions and for which junction parameters the switching distribution is expected to be single mode or

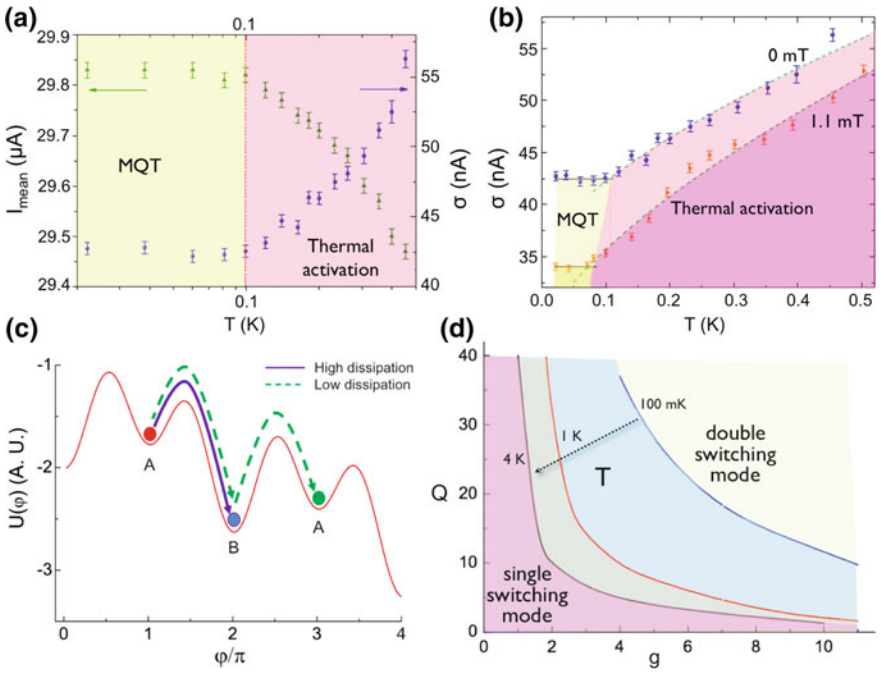


**Fig. 11.20** **a** Temperature behavior of $I_{mean}$ (green up triangles, left axis) and of $\sigma$ (violet circles, right axis) for the NbN/GdN/NbN type of junction in absence of magnetic field. The red dashed line indicates the crossover temperature between MQT regime (dark yellow background) and thermal activation (pink background). In the MQT regime both $I_{mean}$ and $\sigma$ saturate. **b** Comparison between temperature dependences of $\sigma$ at 0 mT (violet circles) and at 1.1 mT (orange right triangles). In presence of magnetic field, lower values of $\sigma$ have been measured and $T_{cr}$ is reduced, according to the theory presented in Sect. 11.1.3. $T_{cr}$ has been determined by the intersection of the $T^{2/3}$ curve in the thermal activation regime (dashed green lines) and the mean value of $\sigma$ in the MQT regime (black full lines). **c** Washboard potential for $g = 2$ and for values of the bias current close to the retrapping current. A and B mark the narrow and the wide potential well, respectively, when tilting the washboard potential from left to right. In case of high dissipation level (blue full line) the phase particle is retrapped in the well B (blue circle), while for low dissipation values (green dashed line) the phase particle can be retrapped in both wells with finite probability (green circle). **d** Phase separation between single and double mode switching distributions, for $g > 0$. Phase separation is temperature dependent, in the figure the curves corresponding to 4 K (black line), 1 K (red line) and 100 mK (blue line) have been reported. The dashed black arrow indicates the direction of temperature increasing. Below the phase separation curve at fixed temperature $T$, the switching distributions are unimodal, while they become bimodal above the phase separation curve. Adapted from [62]

bimodal. Indeed, the heights of the two barriers approach each other when increasing the $g$ factor, and the phase may be retrapped in both the potential wells with a finite probability, resulting in a bimodal switching distribution when counting many escape events. The same occurs when increasing the temperature and the quality factor. As example, a sketch of the washboard potential for $g = 2$ is reported in Fig. 11.20c, where A and B mark the narrow and the wide potential well, respectively, when tilting the washboard from left to right. In case of high dissipation level (blue full line) the phase particle is retrapped in the wider well B (blue circle), while for low dissipation values (green dashed line) the phase particle can be retrapped in both wells A and B with finite probability (green circle) . The results of numerical simulations of the phase dynamics in presence of a double well potential are summerized in Fig. 11.20d, for the case $g > 0$ (the case $g < 0$ will be treated in the next section). Phase separation between single and double mode switching distributions is temperature dependent, in the figure the curves corresponding to 4 K (black line), 1 K (red line) and 100 mK (blue line) have been reported, respectively. Below the phase separation curve at fixed temperature $T$, the switching distributions are unimodal, while they become bimodal above the phase separation curve. More details can be found in [62]. These results are valid for any type of Josephson system with a positive second harmonic component in the $I_s(\varphi)$.

#### 11.3.4.2 SIFS Josephson Junctions

Extensive studies of the phase dynamics in presence of a negative second harmonic component in the $I_s(\varphi)$ have been reported in several works on SIFS JJs [116–118]. The junctions used in these experiments consist of alternating 0 and $\pi$ junctions [92] with asymmetric 0 and $\pi$ regions. The samples are fabricated as $Nb/Al_2O_3/Ni_{0.6}$ $Cu_{0.4}/Nb$ SIFS heterostructures and have an overlap geometry, as shown in Fig. 11.21a. It is well known [107] that the critical current in SFS or SIFS JJs strongly depends on the thickness $d_F$ of the F layer and can become negative within some range of $d_F$ values ($\pi$ junction). Therefore, each junction consists of two parts, a conventional 0 segment and a $\pi$ segment. To produce the 0 and the $\pi$ segments, the F layer has different thicknesses $d_{F,0}$ and $d_{F,\pi}$, as shown in Fig. 11.21a. The effective current-phase relation can be written as [116]:

$$I_s(\varphi) = I_c \left[\sin\varphi + \Gamma_0/2 \sin(2\varphi) + \Gamma_H H \cos\varphi\right] , \tag{11.18}$$

where $\Gamma_0$ and $\Gamma_H$ depend on the lengths $L_0$ and $L_\pi$ and on the critical current densities $J_0$ and $J_\pi$ of both 0 and $\pi$ parts. $H$ is an external magnetic field, which introduces a $\cos\varphi$ term in the $I_s(\varphi)$, if compared with the case discussed in Sect. 11.3.1.1. The current phase relation of (11.18) corresponds to a $\varphi$ JJ at zero magnetic field, since $\Gamma_0$ is negative in an alternating 0-$\pi$ junction [92, 116], thus the JJ has a degenerate ground state phase $\psi = \pm\varphi$ as shown in Fig. 11.21b. In particular, $\varphi$ JJs have been proposed as on-chip phase batteries for biasing various classical and quantum circuits, allowing for removing external bias lines and reducing decoherence [116, 117].

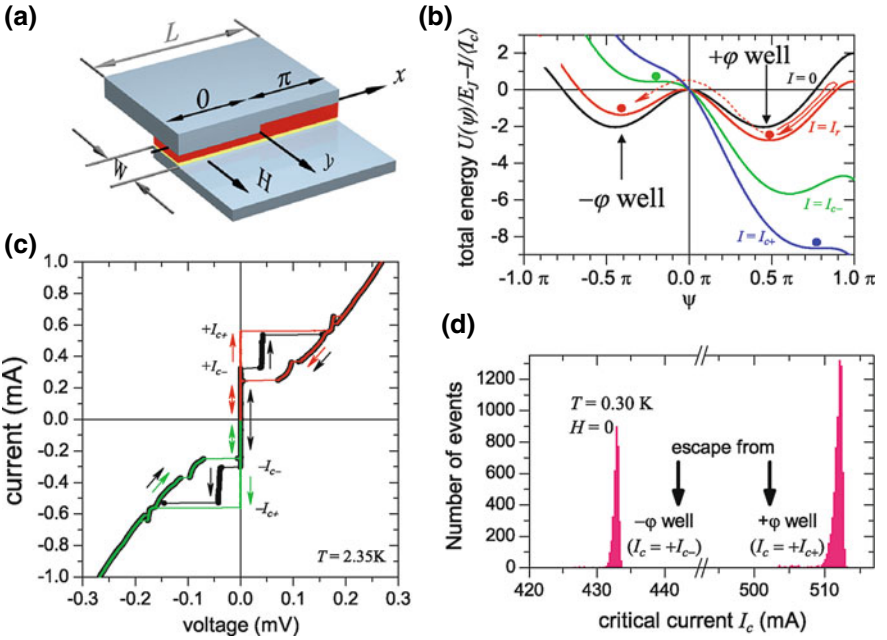


**Fig. 11.21** **a** Sketch of the SIFS $\varphi$ JJ. $L = 200\,\mu$m and $w = 10\,\mu$m $<< L$. The step in the F-layer thickness serves to realize a 0 and a $\pi$ segment. **b** Numerically calculated effective Josephson energy of a $\varphi$ JJ at $H = 0$ tilted by an applied bias current $I > 0$. Different cases are reported: ground state $I = 0$ (black curve), $I = I_r$ (retrapping current, red curve), $I = I_{c-}$ (escape from $-\varphi$ well, green curve), and $I = I_{c+}$ (escape from $+\varphi$ well, blue curve). **c** I-V characteristic showing lower $\pm I_{c-}$ and higher $\pm I_{c+}$ measured at $T \simeq 2.35$ K. At this temperature the behavior is deterministic (see the text). **d** Escape histogram measured at $H = 0$ and $T = 0.3$ K, which shows two peaks corresponding to the two critical currents $+I_{c\pm}$. From [116, 118]

The physics of $\varphi$ JJs is quite unusual. In particular in absence of magnetic field, one should observe two critical currents, corresponding to the escape of the phase from the left ($-\varphi$) or the right ($+\varphi$) well of the double-well Josephson energy potential. The $I_c$ values are different because the maximum slope (maximum supercurrent in Fig. 11.21b) on the right-hand side (positive bias) of the $-\varphi$ well is smaller than the maximum slope on the right-hand side of the $+\varphi$ well, see Fig. 11.21b.

In [92] a technique that allows to choose which $I_c$ is measured has been proposed. The control is done by choosing a proper bias sweep sequence. For example, if the junction is returning from the positive voltage state, the washboard potential is tilted so that the phase slides to the right. When the tilt becomes small enough, then the phase will be trapped, presumably in the right $+\varphi$ well because the phase particle sees a larger potential well. Then, by sweeping the bias in the positive direction, escape from $+\varphi$ (to the right) at $I_{c+}$ should be observed, while in the negative direction escape from $+\varphi$ well (to the left) should lead to the observation of $-I_{c-}$. Definitions of $I_{c+}$, $I_{c-}$, $-I_{c+}$, $-I_{c-}$ are shown in Fig. 11.21c. However, this assumption is not

always true, because of the temperature dependence of the damping factor. Depending on the damping and on the temperature, one can achieve deterministic behavior as described above. In particular, this occurs when damping is small enough to observe the lower $I_c$ but large enough to trap the phase in a particular well [116]. An example of I-V characteristic with deterministic behavior is shown in Fig. 11.21c at $T = 2.35$ K. It is important to note here that, in the frequency dependent damping framework, the quality factor $Q$ in the retrapping process is the low frequency damping in the running state of the JJ (see Fig. 11.18d), which mainly depends on the low voltage resistance of the junction [65]. Values of $Q(\omega \simeq 0) \approx 10$ have been reported in [118] at $T = 2.35$ K.

In the experiment reported in [116], at $T \leq 2.3$ K, when the damping is reduced, the currents $\pm I_{c+}$ and $\pm I_{c-}$ are traced in random order. Recording one I-V characteristic after the other, all four possible combinations are obtained. Therefore, choosing a specific sweep sequence as described above does not make the outcome predictable. In this temperature range the damping is so low that, upon returning from the positive voltage state, the phase does not simply stop in the $+\varphi$ well, but can also reflect from the barrier and find itself in a $-\varphi$ well. The absence of determinism suggests that this system exhibits chaotic dynamics [117]. In the limit of low damping, the $\varphi$ JJ exhibits a butterfly effect, i.e. the destination well strongly depends on the damping. This leads to an impossibility to predict the final well, since in the limit of small damping the destination well is extremely sensitive to the initial conditions: a tiny variation (or fluctuation), for instance thermal or electronic noise, results in a global effect, the retrapping in a different well.

The question at which of the two minima $-\varphi$ or $+\varphi$ the phase will be trapped upon return from a finite voltage state during quasistatic decrease of the bias current, can be addressed by measuring the relative population of the two peaks in the escape histogram [118]. The measurement of the SCDs ($I_{c-}$ or $I_{c+}$) can be used as a simple way to read out an unknown state ($-\varphi$ or $+\varphi$) of the $\varphi$ JJ, since the relative number the phase was trapped and then escapes from the $\pm\varphi$ well is proportional to the number of events $N_{\pm}$ in the corresponding peak in the switching histogram. An example is shown in Fig. 11.21d. By measuring the probability of phase trapping for different temperatures, it turns out that a crossover from the deterministic behavior of the probability to be trapped in the $-\varphi$ well, $P_-(T) = 0$ at high temperature $T > T^*$, to an oscillating finite probability $P_-(T)$, at the onset of the butterfly effect, occurs below a transition temperature $T^* \simeq 2.25$ K [118]. This probability saturates at a value different from 50% at low temperatures; even at very low temperatures $P_-(T)$ saturates at about 0.33 instead of 0.5 predicted theoretically. The simplest and most likely reason for such observation has been ascribed to the saturation of the damping factor at low temperatures caused, for instance, by leakage currents in the barrier [118].

The phase dynamics has been also investigated in other types of SIFS underdamped JJs by measuring the switching probability in both the stationary and non stationary regimes [119]. Large area SIFS tunnel junctions composed by Nb superconducting electrodes, $Al_2O_3$ insulating barrier and PdNi alloy with 10% Ni ferromagnetic layer, have been measured down 350 mK. In the stationary regime, when

the current bias frequency is much smaller than the inverse phase relaxation time $\tau_\varphi{}^{-1}$, the mean switching current and the standard deviation follow the expected temperature behavior in the underdamped regime with no evidence of additional spin noise [119]. Instead, in the nonstationary limit when the bias frequency is comparable to $\tau_\varphi{}^{-1}$, the mean switching current has a finite probability to jump to zero. Therefore, an incomplete energy relaxation leads to dynamical phase bifurcation, which manifests itself as premature switching, resulting in a bimodal switching distribution [119]. By varying the bias frequency, it is possible to directly measure the phase relaxation time.

#### 11.3.4.3 SFS Josephson Junctions

Static properties of fully metallic SFS junctions have been extensively studied in recent years as a model system exhibiting triplet superconductivity [106–109]. To gain deeper insights into the phase dynamics of these types of ferromagnetic junctions, it is important to recall the dynamics of SNS JJs, where N is a normal metal. The energy scale which sets the critical current $I_c$ of an SNS junction is either the energy gap of the superconductor $\Delta$ or the Thouless energy [120–122] $E_{Th} = \hbar D_{diff}/L^2$, as discussed in Chap. 3. In mesoscopic transport terminology, JJs are defined short when $E_{Th} > \Delta$, while long for $E_{Th} < \Delta$ [120–122]. The Thouless energy also determines the minigap $E_g$ appearing in the density of states of the normal metal due to the proximity effect from the two superconducting electrodes [122, 123].

Quantum decay of the supercurrent and intrinsic capacitance contributions have been considered beyond the tunnel limit [123] to deal with the problem of overheating in an SNS junction [124] and of the mismatch between the amplitude of the hysteresis and the calculated capacitance. At low temperatures, the dynamics of the phase is massive and is determined by the effective capacitance, which is the sum of the geometric capacitance, due to the dielectric nature of the barrier, and of the intrinsic capacitance of the junction, introduced in [123, 125] to include the response of Andreev bound states to nonstationary boundary conditions beyond the tunneling limit. The central part of the JJ has been modeled either by an arbitrary short mesoscopic conductor described by the set of its transmission coefficients, or by a diffusive wire of an arbitrary length. The intrinsic capacitance can be generally estimated as $C_i \approx G/E_g$ where $G$ is the normal-state conductance of the junction [123]. Even in the case of negligible geometric capacitance, as in SNS JJs, the obtained $C_i$ is sufficiently large to qualitatively explain the hysteretic behavior of the I-V characteristic, also in absence of overheating. Therefore the intrinsic junction capacitance due to the dynamics of the Andreev bound states may itself lead to hysteretic behavior, even for a perfect thermal contact with the environment [123].

The same arguments apply to pure metallic SFS JJs with multiple misaligned F layers, since in these structures an equal-spin triplet component is induced that can penetrate the F region over distances comparable to $\xi_N$, as in the case of a normal metal [106]. First observation of hysteresis in the I-V curves of fully metallic SFS junctions has been reported in [70], where the barrier only involved a single weak

ferromagnet. Nb-CuNi-Nb moderately damped junctions have been investigated and compared with junctions with different barriers but similar junction parameters, as low ohmic Nb-Pt-Nb (SNS) junctions and Nb-InAs-Nb (S-two dimensional electron gas-S) structures, as discussed in Sect. 11.2. The origin of hysteresis has been explained by considering the large overlap capacitance ($\simeq$35 pF) arising from the specific junction geometry, where the weak ferromagnetic CuNi layer acts as a ground plane for the JJ.

A comprehensive electrodynamic characterization has been later addressed in SFS JJs with Nb electrodes and multiple F barriers [126], using a combination of the strong ferromagnet Co and spiral magnetic Ho layers, which represent the model system exhibiting triplet superconductivity [106, 108, 109, 127]. A sketch of a trilayer structure (Ho/Co/Ho) JJ is shown in Fig. 11.22a along with a typical I-V characteristic. Figure 11.22b shows the temperature dependence of $I_c$ measured on a bilayer structure (Ho/Co) JJ, while in panel (c) of the same figure a set of SCDs measured on the same junction as a function of the temperature, from 0.3 K up to 1.9 K, is reported. The temperature dependence of $I_c$ is typical of long SNS JJs and the fit of the high temperature region according to the Usadel model provides an estimate of the Thouless energy of the order of 25 $\mu$eV (orange curve). Details on the fit can be found in [121, 126]. Due to the strong temperature dependence of the critical current and to the very low values of the ratio $\sigma/I_c \simeq 10^{-3}$, the SCDs cover a very large range of switching currents and are quite narrow. In this temperature range, the behavior of the SCDs is typical of moderately damped JJs [65–68, 70, 74]: the standard deviation $\sigma$, shown in Fig. 11.22d, increases in the temperature range from 0.3 K up to 1.4 K, then it starts to collapse indicating the transition to the PD regime. The transition temperature $T^*$ between the TA and the PD regime is about 1.4 K. The temperature behavior of $\sigma$ can be reproduced through Monte Carlo simulations of the phase dynamics: the fitting parameter is the quality factor $Q$ at 0.3 K, which regulates the collapse of $\sigma$ and the transition temperature $T^*$ as discussed in Sect. 11.3.2. In contrast to previous works, in the simulations the quality factor here is temperature dependent, reflecting the strong temperature dependence of $I_c$ [126]. At higher temperatures $Q(T)$ scales as $\sqrt{I_c(T)}$, to assure consistency between the two quantities. The best fit is shown as the blue curve in Fig. 11.22d with $Q = 1.46$ at 0.3 K, $Q = 1.12$ at $T^*$ and $Q = 0.87$ at 1.9 K. Above this temperature hysteresis is almost zero. According to numerical simulations reported in [65], the I-V characteristic is hysteretic for $Q \geq 0.84$, providing a further proof of the consistency of the Monte Carlo fit. Almost the same temperature behavior of the SCDs has been observed in other bilayer and trilayer SFS JJs [126].

Therefore, measurements of SCDs on pure metallic ferromagnetic JJs with misaligned F layers point to a moderately damped dynamics with a $Q$ factor slightly larger than 1. Such a large value of $Q$ for an SF(N)S JJ can be explained by considering that, while geometric capacitance in these types of structures can be very small, the presence of Andreev bound states in the N (F) layer yields additional capacitance-like contributions, which can dominate over the geometric capacitance [121, 123, 125]. The intrinsic capacitance can generally be estimated as [123] $C_i = a_c\hbar/(R_nE_g)$, where the $a_c$ coefficient is of the order of 0.9 for long junctions [123]. In that limit,

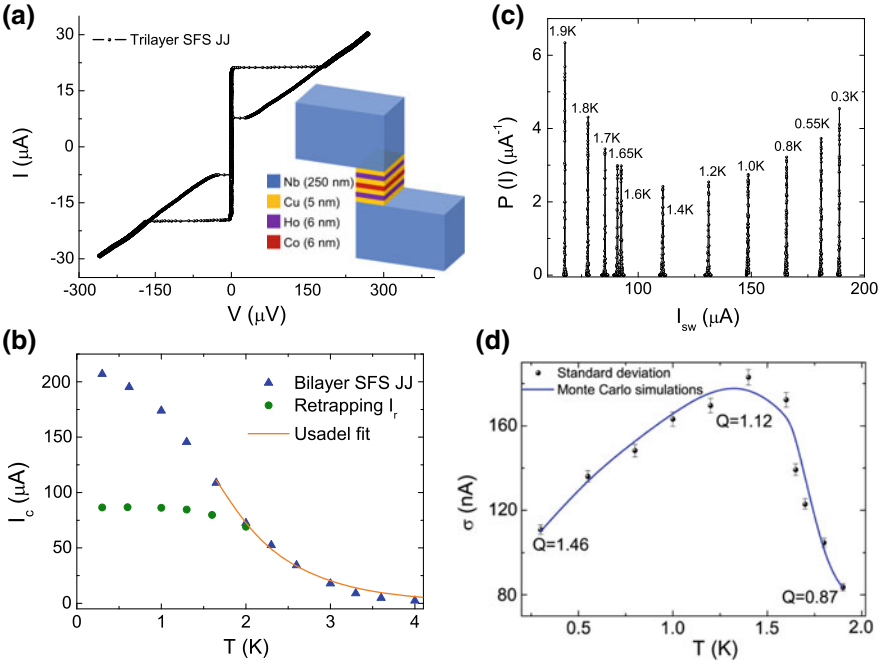


**Fig. 11.22** **a** I-V characteristic of a trilayer JJ measured at 0.3 K. The inset shows a sketch of a typical trilayer (Ho/Co/Ho) junction with the corresponding layer thicknesses. **b** $I_c(T)$ measurements of a bilayer (Ho/Co) JJ (blue triangles). The orange curve is the Usadel fit for $T \geq 1.5$ K and provides an estimation of the Thouless energy of about 25 μeV. The retrapping current $I_r$ is shown by the green circles. For $T \geq 2$ K, $I_r = I_c$ and no hysteresis is present in the I-V characteristics. **c** Measurements of SCDs as a function of the temperature are shown for the bilayer junction reported in panel (**b**). The lines are guides for the eye. A clear transition from the TA to the the PD regime occurs at about 1.4 K. **d** Temperature behavior of the standard deviation $\sigma$ (black dots). The blue line is the fit obtained by Monte Carlo simulations of the phase dynamics, with a quality factor $Q = 1.46$ at 0.3 K. At $T^* = 1.4$ K $Q = 1.12$ and at 1.9 K $Q = 0.87$. Above 2 K the I-V curves are non-hysteretic, see panel (**b**). From [126]

$E_g = 3.12\, E_{Th}$, therefore from the Thouless energy estimated by the $I_c(T)$ fit reported in Fig. 11.22b, values of $E_g \simeq 77$ μeV and $C_i \simeq 8$ pF are obtained [126]. In SNS junctions, where the $R_n$ resistance is of the order of a few Ω or less, the shunting by the high frequency impedance of the circuitry is avoided, thus the effective damping is dominated by $R_n$ itself. By considering the values of $Q$ from the $\sigma(T)$ fit and of $C_i$, it results an effective resistance of about 0.7 Ω, which is very close to the $R_n$ value of the bilayer junction analyzed in Fig. 11.22 ($\simeq 0.6$ Ω) [126].

### 11.3.5 SCDs in Junction with Graphene Barriers

One of the leading ideas of this chapter built on the capability to characterize the phase dynamics of the junctions through measurements of SCDs and the study of fluctuations, has been to show how coupling of the junction to the environment independently of its nature cannot spoil macroscopic quantum phenomena when the junction is in the underdamped or moderately damped regime, i.e. in the appropriate dissipation regime. In some cases the final aim is not necessarily the lowest possible dissipation level, but the capability of the junction to communicate with the environment paying the lowest price in terms of harmful dissipation. Within this framework, a ferromagnetic barrier is by far less convenient than the standard $AlO_x$ barrier in terms of dissipation, but it could offer alternative means to tune the state and the scaling energy of the junction. Along this line of thinking, the damping parameter of the junction has been tuned in different manners by changing temperature, magnetic field and gate voltage and introducing a ferromagnetic layer or in situ capacitive shunting. We complete this overview by mentioning the measurements of SCDs on junctions with other unconventional barriers made of graphene [128].

In junctions composed by superconducting PbIn electrodes and single-layer graphene barriers, prepared by mechanical exfoliation of natural graphite using scotch tape technique [128], a crossover from classical to quantum regime is controlled by the gate voltage and has been found surprisingly high of the order of a few hundreds mK. Observation of this gate tunability of the quantum phenomena is mainly due to the gate-tunable Josephson coupling energy in graphene based JJs. Because the Thouless energy $E_{Th} \simeq 80\,\mu\text{eV}$ is much smaller than the gap $\Delta_{PbIn} =$ 1.1 meV, the junctions fall in the long diffusive limit. $Q$ factor is about 5–6 for all gate voltages. Capacitance is for instance about 35 fF at $V = -60$ V and seems to be not related to self-heating [124] but consistent with an effective capacitance $C_{eff} = \hbar/(\mathrm{R}_n \mathrm{E}_{Th})$, whose origin is attributed to diffusive motion of quasiparticles in graphene [129], in the sense that the charge relaxation time $R_nC$ is replaced by the diffusion time of Andreev pairs $\hbar/E_{Th}$, as discussed in Sect. 11.3.4.3 and in [121, 123, 125]. The capacitance is gate-tunable, following the scaling of $R_n$ with the applied gate voltage [128]. Typical fingerprints of the PD regime, such as the collapse of $\sigma$ above a transition temperature $T^*$, have been found for all gate voltages with $T^*$ ranging from about 1 K ($V = 0$ V) to 2 K ($V = -60$ V).

## 11.4 SCDs in Junctions with High Values of $J_c$

In most of the junctions presented up to now, especially in cases where MQT has been demonstrated, the critical current density $J_c$ is relatively low, not larger than $10^2$–$10^3$ A/cm$^2$. We have already mentioned in Chap. 7 the substantial failure of describing the shape of I-V curves with a set of self-consistent parameters for junctions with high $J_c$. The amplitude of the hysteresis is not consistent with a reliable value of

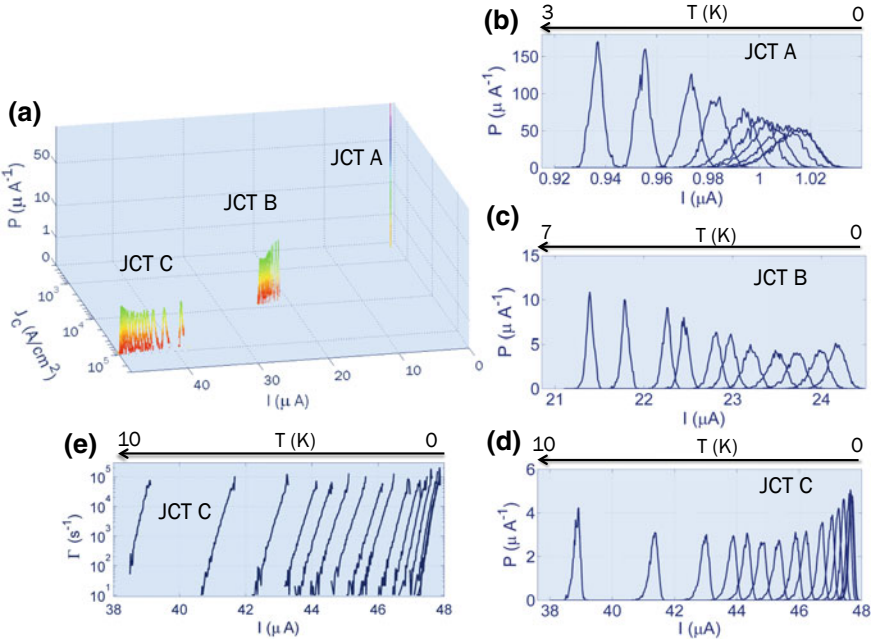


**Fig. 11.23** **a** 3-D graph of the SCDs measured for various temperatures on three GB YBCO JJs. **b** At low $J_c$ values ($5{\cdot}10^2$ A/cm$^2$), the SCDs of junction A are confined to a small range of currents, with $\sigma$ of the order of 10 nA. With increasing $J_c$ the histograms progressively cover a larger interval of currents (junctions B and C in panels **c** and **d** respectively). In panel **e** the escape rate curves $\Gamma(I)$ computed from the SCDs of junction C have been shown in the same temperature range as in panel (**d**). From [86]

the capacitance. This is well established since early times on Nb/AlO$_x$/Nb JJs [130, 131]. This is true also if the junction exhibits ideal Fraunhofer pattern.

Anomalous behavior of the escape rate out of the zero-voltage state has been studied in YBaCuO GB JJs with a high critical current density $J_c$ [86]. These junctions span a wide range of $J_c$ and have appropriate electrodynamic parameters. Such high $J_c$ JJs, when hysteretic, do not switch from the superconducting to the normal state following the expected stochastic Josephson distribution, despite having standard Josephson properties such as a Fraunhofer magnetic field pattern. SCDs are consistent with non-equilibrium dynamics taking place on a local rather than a global scale [86]. This regime apart from its intrinsic interest because of some advantages of very transparent barriers, is also of reference for a growing literature on switching measurements of superconducting nanowires, as discussed in Sect. 11.4.1. The extension of what is known on the Josephson effect for large $J_c$ might be of major interest also for the community searching quantum phase slips and robust protocols to operate nanowires as detectors.

A comparative study of BP GB junctions with different $I_c$ and $J_c$ is presented in Fig. 11.23, where histograms of junctions A ($J_c \simeq 5 \cdot 10^2$ A/cm$^2$), B ($J_c \simeq 10^3$

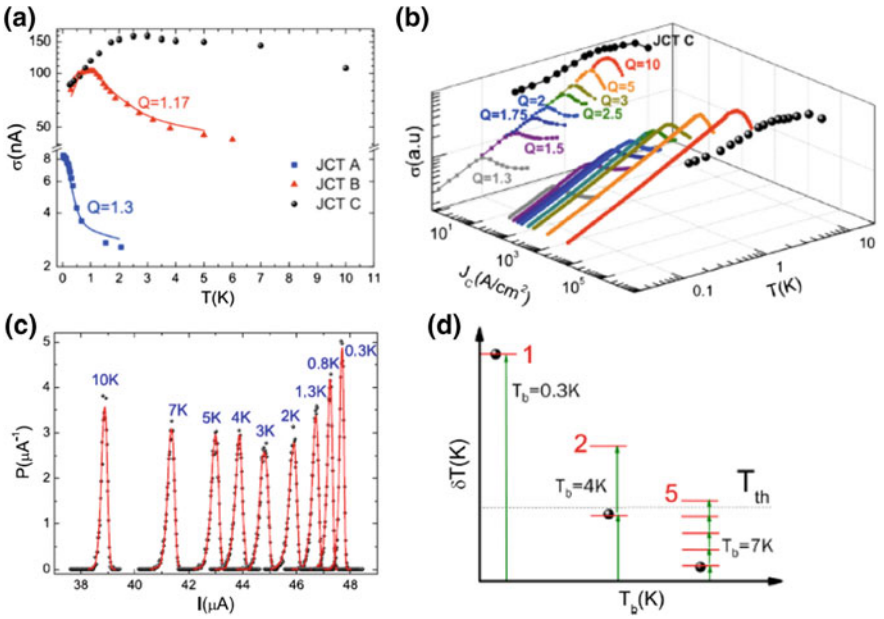


**Fig. 11.24** **a** Temperature dependence of $\sigma$ measured on GB junctions A (blue squares), B (red triangles) and C (black points) respectively. The blue and red solid lines are Monte Carlo simulations of the phase dynamics in the MDR, with $Q = 1.30$ and 1.17 for junctions A and B respectively. **b** Simulations of the temperature dependence of $\sigma$ as a function of $J_c$ for different values of the $Q$ damping parameter (full color lines), confined to the MDR, are compared with experimental data of junction C (black points). Keeping all the other junction parameters fixed, an enhancement of $J_c$ leads to an increase of $I_c$ and $Q$. An increase in $Q$ produces steeper $\sigma$ tails above $T^*$ and cannot reproduce the broadened experimental data of junction C. This is even more evident in the two dimensional $(\sigma - T)$ projection. **c** Measurements of SCDs of junction C (black points) as a function of the temperature. The red lines represent the results of numerical simulations based on multiple heating events, as explained in the text. In panel **d** the arrows qualitatively sketch the temperature jump due to a single heating event and the number of events necessary to induce the switching to the resistive state, which increases as the temperature increases. $T_{th}$ is the threshold temperature above which the transition to the resistive state occurs. From [86]

A/cm$^2$) and C ($J_c \simeq 10^5$ A/cm$^2$) are shown. The 3-D view gives an intuitive picture: SCDs cover distinct current ranges, and when $J_c$ increases, they become broader. In the right part of the figure, each set of SCDs is displayed with appropriate scales for a better view of the details of their temperature dependence. In Fig. 11.23e the escape rate $\Gamma(I)$ out of the zero-voltage state has been plotted for junction C in the same temperature range [86]. The standard deviation $\sigma$ of the histograms is reported for all junctions in Fig. 11.24a. The $\sigma(T)$ behaviors of junctions A and B match well the predictions of the RSJ model for moderately damped JJs, as discussed in the previous sections and extensively in [86]. Both junctions A and B show the transition to the PD regime, in which the derivative $d\sigma/dT$ is negative. In junction B the transition from TA to the PD regime is observed, while for junction A a direct transition from

MQT to the PD regime is found [77]. In both junctions A and B the rate of decrease in $\sigma$ above $T^*$ with increasing $T$ is well described by the Monte Carlo fit of the phase dynamics (blue and red solid lines in Fig. 11.24a, respectively).

Junction C is characterized by high values of $J_c$ close to those observed in superconducting nanowires (see Sect. 11.4.1). This device exhibits radically different phase dynamics above 3 K, which represents a transition temperature $T^{**}$ [86]. The rate of decrease of $\sigma$ above $T^{**}$ turns to be a distinctive marker of the phase dynamics. In device C the slope of $\sigma(T)$ above $T^{**}$ is much smaller when compared to those of junctions A and B and cannot be described in terms of the moderately damped regime. According to the RSJ model, keeping all the other junctions parameters fixed, an increase of $J_c$ leads to an enhancement of $I_c$ and $Q$. The increase of $Q$ moves $T^*$ to higher values, and the negative slope of $\sigma(T)$ above $T^*$ becomes steeper and steeper, as shown by the numerical simulations for $Q$ ranging between 1 and 10 reported in Fig. 11.24b [86]. In addition, while moderately damped JJs show a progressive symmetrization of the switching histograms near to and above $T^*$, SCDs of junction C are asymmetric over the entire temperature range. In junction C, the $\gamma$ factor is temperature independent [86]. These behaviors are quite distinct and do not fall in the framework of any regime of the RSJ model.

The absence of a set of self-consistent electrodynamic parameters to describe junction C is a strong indication of the failure of the standard Josephson dynamics. This failure is of general relevance, applying both to conventional low $T_c$ JJs [130, 131] and to the emergent class of hybrid nanoscale junctions (see for instance Chap. 13). For larger values of $J_c$, the switching dynamics can be described in terms of heating driven mechanisms, which become dominant with a transition to the normal state locally in the junction area. These events, which have been firstly considered in the dynamics of superconducting nanowires, are the mirror of non-equilibrium processes and can be modeled as "phase slips entities" (PSEs), in the sense that they are local processes, break the coherence of the phase information and are described by a heat diffusion-like equation. In particular, the probability for a single heating event can be still described in terms of the Langer-Ambegaokar-McCumber-Halperin (LAHM) theory [132, 133] and further extensions [134], and PSEs can still be approximately assumed to be far apart in time.

Following an approach proposed in [135] for LTS nanowires, numerical simulations of the temperature jump induced by a PSE obey the phenomenological diffusive equation for the relaxation of the temperature gradient:

$$\frac{d\delta T}{dt} + \alpha\,(T, T_b)\;\delta T = r(T_b, t) + \eta(T, I)\sum_i \delta(t - t_i)\,. \tag{11.19}$$

Here $\delta T = T - T_b$ is the deviation from the temperature of the bath $T_b$. The relaxation coefficient $\alpha\,(T, T_b)$ depends on the thermal conductivity $K(T)$, on the thermal capacity $\mathcal{C}_v(T)$ of the phase slip volume, and on $T_b$. $r(T_b, t)$ is the noise source due to the environment with an admittance $Y(\omega)$, while $\eta(T, I)$ is the temperature jump due to the PSEs which occur at the stochastically distributed times $t_i$. $\eta(T, I)$

is implicitly defined by the following equation:

$$E_{PSE} = \phi_o I = \int_T^{T+\eta(T,I)} dT' \; C_v(T'), \tag{11.20}$$

where $E_{PSE}$ is the energy dissipated by a PSE. The SCDs derived from the experiment on junction C over a wide temperature range are reported in Fig. 11.24c. The continuous red curves correspond to the fit obtained integrating (11.19). In [86] it is also carefully described the procedure used to quantify how many heating events are needed to escape to the finite voltage state.

A single heating event can induce a direct jump to the resistive state at low temperatures: it induces a large local heating that is difficult to dissipate. The system is not at equilibrium with its environment, and the effective temperature $T_{eff}$ for the system higher than $T_b$. At high temperatures the opposite regime of small $\eta$(T) per heating event takes place (see Fig. 11.24d). In addition both the thermal conductivity $K(T)$ and the thermal capacity $C_v(T)$ increase with increasing temperature as well. Thermal diffusion and contact with the environment is more effective and multiple PSEs are required for switching. This occurs above $T^{**}$, where the derivative $d\sigma/dT$ is negative. $T_{eff}$ and $T_b$ coincide above $T^{**}$, which is interpreted as the temperature at which the system is able to thermalize during the time interval between well separated heating events. Experimental SCDs complemented by the numerical simulations follow the passage from single to multiple heating events. A consistent set of the junction parameters (temperature jump $\eta$, number of heating events) can be extracted from the simulations [86].

Therefore, a heat diffusion-like model breaking phase-coherent information is consistent with measurements of SCDs on high $J_c$ JJs. Here the switch to the normal state is accompanied by a local release of energy characteristic of a PSE. When departing from the supercurrent branch, non-equilibrium processes produce an unexpected heating. This is different from what commonly is accepted for hysteretic JJs, where heating can only influence the retrapping phenomena [124], due to Joule power dissipation in the resistive state.

Some analogies can be established with what is observed in $^4$He superfluid [136]. Here the passage from weak to strong coupling manifests itself in a change in the current-phase relation. In the strong coupling regime, where the healing length of the superfluid is lower than the diameter of the constriction, deviations from the $\sin\varphi$ relation appear, while sinusoidal Josephson oscillations have been measured in the opposite limit [136]. An increase in $J_c$ and in the coupling between the electrodes leads to the presence of other harmonics in the current-phase relation, which might become multivalued [137].

Recently, the highly transparent barrier regime nominally leading to high $J_c$ values has been investigated also theoretically [138, 139]. The key differences from the Hamiltonian reported in (1.10) consist of a different expression of the potential energy, because of the Andreev bound states determining $I_c$ (see 1.46), and of an additional term describing subgap Andreev levels forming an effective environment for the Josephson phase. The environment is described by a certain number of har-

monic oscillators with defined frequencies coupled to the "particle coordinate" $\varphi$ [138, 139]. The behavior of highly transparent superconducting weak links can be in many respects different from those of conventional Josephson tunnel barriers. An example is a non-trivial non-monotonic dependence of the SCDs on the temperature, which has been predicted in MQT experiments. Furthermore, quasiparticles with overgap energies provide extra capacitance renormalization. Hence, the renormalized junction capacitance may differ substantially from the geometric one.

### *11.4.1 SCDs in Nanowires*

Measurements of SCDs have been recently performed on a series of different nanostructures. Some of them are junctions and can be easily classified in the schemes described above, and more specifically in the moderately damped regime. Some of them are simple nanowires. Stochastic dynamics of superconductive-resistive switching in hysteretic current-biased superconducting nanowires undergoing phase-slip [132, 133, 140] fluctuations is a topic of growing interest. A review of the main concepts and results can be found in books [141, 142] and in a series of papers [143, 144]. We will give a brief account only of those concerning SCD measurements, that will turn to be a direct way of discriminating the phase dynamics and the transport in non trivial cases, which are going to be more and more common with advances in nano-patterning superconductors at extreme scales.

Recent studies have reported phase-slip induced switching in superconducting nanowires [143, 145–147]. In these devices, $J_c$ is of the order of $10^6$ A/cm$^2$ and hysteretic I-V characteristics have been usually observed. In all the mentioned works the phase dynamics has been described in terms of the Josephson dynamics. Because of an extremely small capacitance, a nanowire is believed to be heavily overdamped ($Q \ll 1$). Therefore, the origin of hysteresis has been explained in terms of heating that can also lead to hysteretic behavior in overdamped superconducting-normal-superconducting bridges [124]. The common hypothesis is that the dynamics is always overdamped and runaway heating induces the switching to the finite voltage state.

In $Mo_{79}Ge_{21}$ nanowires of length ranging from 100 up to 200 nm [145], SCDs have been used to investigate the behavior of individual quantum phase-slip (QPS) events at high bias currents, observing a monotonic increase of $\sigma$ with decreasing temperature. In Al nanowires [146] of width less than 10 nm and length ranging from 1.5 to 10 $\mu$m (with $I_c$ of the order of a few $\mu$A), the temperature dependence of $\sigma$ exhibits three distinct regions of behaviors and is nonmonotonic in temperature. Saturation is present well below the critical temperature $T_c$, $\sigma$ increases as $T^{2/3}$ at intermediate temperatures, and a collapse is present close to $T_c$. The relationship between individual phase slips and switching has been also theoretically investigated [135] in order to provide a tool to study phase slips, to help establish whether they are caused by thermal fluctuations or by macroscopic quantum tunneling [132]. It has been found that although several phase-slip events are generally necessary to

induce switching, there is an experimentally accessible regime of temperatures and currents for which just one single phase-slip event is sufficient to induce switching, via the local heating it causes.

Highly confined phase slips have been studied through measurements of SCDs also at the contact point of two Al superconducting leads [148], where the nanoconstriction has been shrunk in situ, thus allowing a comparative study on the very same sample. Two distinct thermal regimes have been found. One corresponding to efficient heat removal where the constriction and bath temperatures remain close to each other, and the other in which the constriction temperature can be substantially larger than the bath temperature leading to the formation of a hot spot [148].

The effects of local heating also in junctions has been already discussed in Sect. 11.4. The common model in all these works has two ingredients [135]: stochastic phase slips that heat the wire by a quantum of energy $Ih/2e$, and occur at random times and locations in the wire, but with a rate that depends on the local temperature of the wire; the heat produced by the phase slips is conducted along the wire, and is carried away by the leads.

In some papers QPSs have been claimed as saturation of the standard deviation $\sigma$ below a crossover temperature, in analogy to JJs [146], while in other works the quantum regime has been identified as deviations at low temperatures from the expected TA behavior [145]. Thus, no consensus exists about the conditions under which QPSs occur and which are the fingerprints of the transition to the quantum as far as SCD measurements are concerned. Moreover, there is a lack of a self-consistent check of the scaling of the fundamental parameters in the quantum regime on the same device by using an in-situ knob, such as the magnetic field for a JJ.

## References

1. H.A. Kramers, Brownian motion in a field of force and the diffusion model of chemical reactions. Physica **7**, 284–304 (1940)
2. M. Büttiker, E.P. Harris, R. Landauer, Thermal activation in extremely underdamped Josephson-junction circuits. Phys. Rev. B **28**, 1268 (1983)
3. P. Hanggi, P. Talkner, M. Borkovec, Reaction-rate theory: fifty years after Kramers. Rev. Mod. Phys. **62**, 251 (1990)
4. H. Grabert, U. Weiss, Crossover from thermal hopping to quantum tunneling. Phys. Rev. Lett. **53**, 1787 (1984)
5. Yu.M. Ivanchenko, L.A. Zilberman, Destruction of Josephson current by fluctuations, Zh. Esker. Teor. Fiz. **55**, 2395–2402 (1968); Sov. Phys. JETP **28**, 1272–1276 (1969)
6. A.O. Caldeira, A.J. Leggett, Influence of dissipation on quantum tunneling in macroscopic systems. Phys. Rev. Lett. **46**, 211 (1981)
7. A.O. Caldeira, A.J. Leggett, Quantum tunnelling in a dissipative system. Ann. Phys. **149**, 374–456 (1993)

8. A.O. Caldeira, *An Introduction to Macroscopic Quantum Phenomena and Quantum Dissipation* (Cambridge University Press, Cambridge, 2014)
9. A. Barone, Y.N. Ovchinnikov, Macroscopic quantum tunneling in small- and large-dissipation regimes. J. Low Temp. Phys. **55**, 297–302 (1984)
10. V. Ambegaokar, U. Eckern, G. Schön, Quantum dynamics of tunneling between superconductors. Phys. Rev. Lett. **48**, 1745 (1982)
11. U. Eckern, G. Schön, V. Ambegaokar, Quantum dynamics of a superconducting tunnel junction. Phys. Rev. B **30**, 6419 (1984)
12. A.I. Larkin, Yu.N. Ovchinnikov, Quantum tunneling with dissipation. Zh. Esker. Teor. Pis. Red. **37**, 322–325 (1969); JETP Lett. **37**, 382–385 (1969)
13. H. Grabert, U. Weiss, P. Hanggi, Quantum tunneling in dissipative systems at finite temperatures. Phys. Rev. Lett. **52**, 2193 (1984)
14. G. Schön, A.D. Zaikin, Quantum description of dissipation in normal metals and short constrictions. Phys. Rev. B **40**, 5231 (1989)
15. J.M. Martinis, H. Grabert, Thermal enhancement of macroscopic quantum tunneling: derivation from noise theory. Phys. Rev. B **38**, 2371 (1988)
16. D. Waxman, A.J. Leggett, Dissipative quantum tunneling at finite temperatures. Phys. Rev. B **32**, 4450 (1985)
17. J. Kurkijärvi, Intrinsic fluctuations in a superconducting ring closed with a Josephson junction. Phys. Rev. B **6**, 832 (1972)
18. T.A. Fulton, L.N. Dunkleberger, Lifetime of the zero-voltage state in Josephson tunnel junctions. Phys. Rev. B **9**, 4760 (1974)
19. A. Garg, Escape-field distribution for escape from a metastable potential well subject to a steadily increasing bias field. Phys. Rev. B **51**, 15592 (1995)
20. L.D. Jackel, W.W. Webb, J.E. Lukens, S.S. Pei, Measurement of the probability distribution of thermally excited fluxoid quantum transitions in a superconducting ring closed by a Josephson junction. Phys. Rev. B **9**, 115 (1974)
21. R.F. Voss, R.A. Webb, Macroscopic quantum tunneling in 1-$\mu$m Nb Josephson junctions. Phys. Rev. Lett. **47**, 265 (1981)
22. L.D. Jackel, J.P. Gordon, E.L. Hu, R.E. Howard, L.A. Fetter, D.M. Tennant, R.W. Epworth, J. Kurkijärvi, Decay of the zero-voltage state in small-area, high-current-density Josephson junctions. Phys. Rev. Lett. **47**, 697 (1981)
23. W. den Boer, R. de Bruyn Ouboter, Flux transition mechanisms in superconducting loops closed with a low capacitance point contact. Phys. B+C **98**, 185–190 (1980); D.W. Bol, R. van Weelderen, R. de Bruyn Ouboter, On the conditional transition probabilities of the magnetic flux at low temperatures in a superconducting loop closed with a low-capacitance superconducting point contact. Phys. B+C **122**, 1–7 (1983); D.W. Bol, J.J.F. Scheffer, W. Giele, R. de Bruyn Ouboter, Thermal activation in the quantum regime and macroscopic quantum tunnelling in the thermal regime in a metabistable system consisting of a superconducting ring interrupted by a weak junction: part I: thermal activation in the quantum regime. Phys. B+C **133**, 196–209 (1985)
24. R.J. Prance, A.P. Long, T.D. Clarke, A. Widom, J.E. Mutton, J. Sacco, M.W. Potts, G. Negaloudis, F. Goodall, Macroscopic quantum electrodynamic effects in a superconducting ring containing a Josephson weak link. Nature **289**, 543–549 (1981)
25. I.M. Dimitrenko, V.A. Khlus, G.M. Tsoi, V.I. Shnyrkov, Quantum decay of metastable current states in rf SQUIDs. Fiz. Nizk. Temp. **11**, 146–160 (1985); Sov. J. Low Temp. **11**, 77–90 (1985)
26. S. Washburn, R.A. Webb, R.F. Voss, S.M. Farris, Effects of dissipation and temperature on macroscopic quantum tunneling. Phys. Rev. Lett. **54**, 2712 (1981)
27. D.B. Schartz, B. Sen, C.N. Archie, J.E. Lukens, Quantitative study of the effect of the environment on macroscopic quantum tunneling. Phys. Rev. Lett. **55**, 1547 (1985)
28. M.H. Devoret, J.M. Martinis, D. Esteve, J. Clarke, Resonant activation from the zero-voltage state of a current-biased Josephson junction. Phys. Rev. Lett. **53**, 1260 (1984)
29. M.H. Devoret, J.M. Martinis, J. Clarke, Measurements of macroscopic quantum tunneling out of the zero-voltage state of a current-biased Josephson junction. Phys. Rev. Lett. **55**, 1908 (1985)

30. J.M. Martinis, M.H. Devoret, J. Clarke, Experimental tests for the quantum behavior of a macroscopic degree of freedom: the phase difference across a Josephson junction. Phys. Rev. B **35**, 4682 (1987)
31. J. Clarke, A.N. Cleland, M.H. Devoret, D. Esteve, J.M. Martinis, Quantum mechanics of a macroscopic variable: the phase difference of a Josephson junction. Science **239**, 992–997 (1988)
32. H.W. Ott, *Noise Reduction Techniques in Electronic Systems* (Wiley Interscience, New York, 1988)
33. R. Morrison, *Grounding and Shielding Techniques* (Wiley Interscience, New York, 1998)
34. A.B. Zorin, The thermocoax cable as the microwave frequency filter for single electron circuits. Rev. Sci. Instrum. **66**, 4296–4300 (1995)
35. F.P. Milliken, J.R. Rozen, G.A. Keefe, R.H. Koch, 50 Ω characteristic impedance low-pass metal powder filters. Rev. Sci. Instrum. **78**, 024701–024705 (2007)
36. D.A. Bennett, L. Longobardi, V. Patel, W. Chen, J.E. Lukens, rf-SQUID qubit readout using a fast flux pulse. Supercond. Sci. Tech. **20**, 445 (2007)
37. D. Esteve, M.H. Devoret, J.M. Martinis, Effect of an arbitrary dissipative circuit on the quantum energy levels and tunneling of a Josephson junction. Phys. Rev. B **34**, 158 (1986)
38. P. Silvestrini, S. Pagano, R. Cristiano, O. Liengme, K.E. Gray, Effect of dissipation on thermal activation in an underdamped Josephson junction: first evidence of a transition between different damping regimes. Phys. Rev. Lett. **60**, 844 (1988)
39. E. Turlot, D. Esteve, C. Urbina, J.M. Martinis, M.H. Devoret, S. Linkwitz, H. Grabert, Escape oscillations of a Josephson junction switching out of the zero-voltage state. Phys. Rev. Lett. **62**, 1788 (1989)
40. J.R. Kirtley, C.D. Tesche, W.J. Gallagher, A.W. Kleinsasser, R.L. Sandstrom, S.I. Raider, P.A. Fisher, Measurement of the intrinsic subgap dissipation in Josephson junctions. Phys. Rev. Lett. **61**, 2372 (1988)
41. M.G. Castellano, G. Torrioli, F. Chiarello, C. Cosmelli, P. Carelli, Return current in hysteretic Josephson junctions: experimental distribution in the thermal activation regime. J. Appl. Phys. **86**, 6405–6411 (1999)
42. M.G. Castellano, R. Leoni, G. Torrioli, F. Chiarello, C. Cosmelli, A. Costantini, G. Diambrini-Palazzi, P. Carelli, R. Cristiano, L. Frunzio, Switching dynamics of Nb/AlOx/Nb Josephson junctions: measurements for an experiment of macroscopic quantum coherence. J. Appl. Phys. **80**, 2922–2928 (1996)
43. A. Barone, R. Cristiano, P. Silvestrini, Supercurrent decay in underdamped Josephson junctions: nonstationary case. J. Appl. Phys. **58**, 3822–3826 (1985)
44. Yu.N. Ovchinnikov, A. Barone, A.A. Varlamov, Effect of magnetic field on macroscopic quantum tunneling escape time in small Josephson junctions. Phys. Rev. B **78**, 054521 (2008); Y.N. Ovchinnikov, A. Barone, A.A. Varlamov, Macroscopic quantum tunneling in "Small" Josephson junctions in a magnetic field. Phys. Rev. Lett. **99**, 037004 (2007)
45. A. Wallraff, T. Duty, A. Lukashenko, A.V. Ustinov, Multiphoton transitions between energy levels in a current-biased Josephson tunnel junction. Phys. Rev. Lett. **90**, 370031 (2003)
46. J.E. Marchese, M. Cirillo, N. Grønbech-Jensen, Classical analogs for Rabi-oscillations, Ramsey-fringes, and spin-echo in Josephson junctions. Eur. Phys. J. Spec. Top. **147**, 333–342 (2007); N. Grønbech-Jensen, M. Cirillo, Rabi-type oscillations in a classical Josephson junction. Phys. Rev. Lett. **95**, 067001 (2005); J.E. Marchese, M. Cirillo, N. Grønbech-Jensen, Classical analysis of phase-locking transients and Rabi-type oscillations in microwave-driven Josephson junctions. Phys. Rev. B **73**, 174507 (2006)
47. B. Ivlev, G. Pepe, R. Latempa, A. Barone, F. Barkov, J. Lisenfeld, A.V. Ustinov, Extreme multiphoton phenomena in Josephson junctions: Euclidean resonance. Phys. Rev. B **72**, 094507 (2005)
48. A.I. Larkin, Yu.N. Ovchinnikov, Effect of level quantization on the lifetime of metastable states. Zh. Esker. Teor. Fiz. **91**, 318–325 (1986); Sov. Phys. JETP **64**, 185–189 (1986)
49. A.I. Larkin, Yu.N. Ovchinnikov, Current damping in superconducting junctions with nonequilibrium electron distribution functions. Zh. Esker. Teor. Fiz. **87**, 1842–1856 (1984); Sov. Phys. JETP **60**, 1060–1067 (1984)

50. P. Kopietz, S. Chakravarty, Lifetime of metastable voltage states of superconducting tunnel junctions. Phys. Rev. B **38**, 97 (1988)
51. R. Rouse, S. Han, J.E. Lukens, Observation of resonant tunneling between macroscopically distinct quantum levels. Phys. Rev. Lett. **75**, 1614 (1995)
52. E. Ben-Jacob, D.J. Bergman, B.J. Matkowsky, Z. Schuss, Lifetime of oscillatory steady states. Phys. Rev. A **26**, 2805 (1982)
53. Y.C. Chen, M.P.A. Fischer, A.J. Leggett, The return of a hysteretic Josephson junction to the zero-voltage state: I-V characteristic and quantum retrapping. J. Appl. Phys. **64**, 3119 (1988)
54. E. Ben-Jacob, D.J. Bergman, Y. Imry, B.J. Matkowsky, Z. Schuss, Thermal activation from the fluxoid and the voltage states of dc SQUIDs. J. Appl. Phys. **54**, 6533–6542 (1983)
55. F. Sharifi, J.L. Gavilano, D.J. Van Harlingen, Macroscopic quantum tunneling and thermal activation from metastable states in a dc SQUID. Phys. Rev. Lett. **61**, 742 (1988)
56. S. Han, J. Lapointe, J.E. Lukens, Thermal activation in a two-dimensional potential. Phys. Rev. Lett. **63**, 1712 (1989)
57. V. Lefevre-Seguin, E. Turlot, C. Urbina, D. Esteve, M.H. Devoret, Thermal activation of a hysteretic dc superconducting quantum interference device from its different zero-voltage states. Phys. Rev. B **46**, 5507 (1992)
58. S.-X. Li, Y. Yu, Y. Zhang, W. Qiu, S. Han, Quantitative study of macroscopic quantum tunneling in a dc SQUID: a system with two degrees of freedom. Phys. Rev. Lett. **89**, 098301 (2002)
59. F. Balestro, J. Claudon, J.P. Pekola, O. Buisson, Evidence of two-dimensional macroscopic quantum tunneling of a current-biased dc SQUID. Phys. Rev. Lett. **91**, 158301 (2003)
60. S. Butz, A.K. Feofanov, K.G. Fedorov, H. Rotzinger, A.U. Thomann, B. Mackrodt, R. Dolata, V.B. Geshkenbein, G. Blatter, A.V. Ustinov, Flux-dependent crossover between quantum and classical behavior in a dc SQUID. Phys. Rev. Lett. **113**, 247005 (2014)
61. L. Longobardi, D. Massarotti, G. Rotoli, D. Stornaiuolo, G. Papari, A. Kawakami, G.P. Pepe, A. Barone, F. Tafuri, Quantum crossover in moderately damped epitaxial NbN/MgO/NbN junctions with low critical current density. Appl. Phys. Lett. **99**, 062510 (2011)
62. D. Massarotti, A. Pal, G. Rotoli, L. Longobardi, M.G. Blamire, F. Tafuri, Macroscopic quantum tunnelling in spin filter ferromagnetic Josephson junctions. Nat. Commun. **6**, 7376 (2015)
63. O. Buisson, F. Balestro, J.P. Pekola, F.W.J. Hekking, One-shot quantum measurement using a hysteretic dc SQUID. Phys. Rev. Lett. **90**, 238304 (2003)
64. A. Wallraff, A. Lukashenko, J. Lisenfeld, A. Kemp, M.V. Fistul, Y. Koval, A.V. Ustinov, Quantum dynamics of a single vortex. Nature **425**, 125–128 (2003)
65. R.L. Kautz, J.M. Martinis, Noise-affected I-V curves in small hysteretic Josephson junction. Phys. Rev. B **42**, 9903 (1990)
66. J.M. Kivioja, T.E. Nieminen, J. Claudon, O. Buisson, F.W.J. Hekking, J.P. Pekola, Observation of transition from escape dynamics to underdamped phase diffusion in a Josephson junction. Phys. Rev. Lett. **94**, 247002 (2005)
67. J. Männik, S. Li, W. Qiu, W. Chen, V. Patel, S. Han, J.E. Lukens, Crossover from Kramers to phase-diffusion switching in moderately damped Josephson junctions. Phys. Rev. B **71**, 220509 (2005)
68. V.M. Krasnov, T. Bauch, S. Intiso, E. Hürfeld, T. Akazaki, H. Takayanagi, P. Delsing, Collapse of thermal activation in moderately damped Josephson junctions. Phys. Rev. Lett. **95**, 157002 (2005)
69. J.M. Kivioja, T.E. Nieminen, J. Claudon, O. Buisson, F.W.J. Hekking, J.P. Pekola, Weak coupling Josephson junction as a current probe: effect of dissipation on escape dynamics. New J. Phys. **7**, 179–200 (2005)
70. V.M. Krasnov, T. Golod, T. Bauch, P. Delsing, Anticorrelation between temperature and fluctuations of the switching current in moderately damped Josephson junctions. Phys. Rev. B **76**, 224517 (2007)
71. J.C. Fenton, P.A. Warburton, Monte Carlo simulations of thermal fluctuations in moderately damped Josephson junctions: multiple escape and retrapping, switching- and return-current distributions, and hysteresis. Phys. Rev. B **78**, 054526 (2008)

72. M.-H. Bae, M. Sahu, H.-J. Lee, A. Bezryadin, Multiple-retrapping processes in the phase-diffusion regime of high-Tc intrinsic Josephson junctions. Phys. Rev. B **79**, 104509 (2009)
73. H.F. Yu, X.B. Zhu, Z.H. Peng, Y. Tian, D.J. Cui, G.H. Chen, D.N. Zheng, X.N. Jing, L. Lu, S.P. Zhao, S. Han, Quantum phase diffusion in a small underdamped Josephson junction. Phys. Rev. Lett. **107**, 067004 (2011)
74. L. Longobardi, D. Massarotti, G. Rotoli, D. Stornaiuolo, G. Papari, A. Kawakami, G.P. Pepe, A. Barone, F. Tafuri, Thermal hopping and retrapping of a Brownian particle in the tilted periodic potential of a NbN/MgO/NbN Josephson junction. Phys. Rev. B **84**, 184504 (2011)
75. Y. Yoon, S. Gasparinetti, M. Mottonen, J.P. Pekola, Capacitively enhanced thermal escape in underdamped Josephson junctions. J. Low Temp. Phys. **163**, 164–169 (2011)
76. H. Grabert, G.-L. Ingold, B. Paul, Phase diffusion and charging effects in Josephson junctions. Europhys. Lett. **44**, 360–366 (1998)
77. L. Longobardi, D. Massarotti, D. Stornaiuolo, L. Galletti, G. Rotoli, F. Lombardi, F. Tafuri, Direct transition from quantum escape to a phase diffusion regime in YBaCuO biepitaxial Josephson junctions. Phys. Rev. Lett. **109**, 050601 (2012)
78. F. Tafuri, J.R. Kirtley, Weak links in high critical temperature superconductors. Rep. Prog. Phys. **68**, 2573–2663 (2005)
79. Y.V. Fominov, A.A. Golubov, M.Y. Kupriyanov, Decoherence due to nodal quasiparticles in d-wave qubits. Pis'ma v Zh. Eksp. Teor. Fiz. **77**, 691–695 (2003); JETP Lett. **77**, 587–591 (2003); M.H.S. Amin, A.Y. Smirnov, Quasiparticle Decoherence in d-Wave Superconducting Qubits. Phys. Rev. Lett. **92**, 017001 (2004)
80. S. Kawabata, S. Kashiwaya, Y. Asano, Y. Tanaka, Macroscopic quantum tunneling and quasiparticle dissipation in d-wave superconductor Josephson junctions. Phys. Rev. B **70**, 132505 (2004); S. Kawabata, S. Kashiwaya, Y. Asano, Y. Tanaka, Effect of zero-energy bound states on macroscopic quantum tunneling in high-Tc superconductor junctions. Phys. Rev. B **72**, 052506 (2005); T. Yokoyama, S. Kawabata, T. Kato, Y. Tanaka, Theory of macroscopic quantum tunneling in high-$T_c$ $c$-axis Josephson junctions. Phys. Rev. B **76**, 134501 (2007)
81. T. Bauch, F. Lombardi, F. Tafuri, A. Barone, G. Rotoli, P. Delsing, T. Claeson, Macroscopic quantum tunneling in $d$-wave $YBa_2Cu_3O_{7-x}$ Josephson junctions. Phys. Rev. Lett. **94**, 087003 (2005)
82. T. Bauch, T. Lindström, F. Tafuri, G. Rotoli, P. Delsing, T. Claeson, F. Lombardi, Quantum dynamics of a d-wave Josephson junction. Science **311**, 57–60 (2006)
83. G. Rotoli, T. Bauch, T. Lindstrom, D. Stornaiuolo, F. Tafuri, F. Lombardi, Classical resonant activation of a Josephson junction embedded in an LC circuit. Phys. Rev. B **75**, 144501 (2007)
84. S. Kawabata, T. Bauch, T. Kato, Theory of two-dimensional macroscopic quantum tunneling in $YBa_2Cu_3O_{7-x}$ Josephson junctions coupled to an LC circuit. Phys. Rev. B **80**, 174513 (2009)
85. D. Massarotti, L. Longobardi, L. Galletti, D. Stornaiuolo, D. Montemurro, G.P. Pepe, G. Rotoli, A. Barone, F. Tafuri, Escape dynamics in moderately damped Josephson junctions. Low Temp. Phys. **38**, 263 (2012); Fiz. Nizk. Temp. **38**, 336–347 (2012)
86. D. Massarotti, D. Stornaiuolo, P. Lucignano, L. Galletti, D. Born, G. Rotoli, F. Lombardi, L. Longobardi, A. Tagliacozzo, F. Tafuri, Breakdown of the escape dynamics in Josephson junctions. Phys. Rev. B **92**, 054501 (2015)
87. D. Stornaiuolo, G. Papari, N. Cennamo, F. Carillo, L. Longobardi, D. Massarotti, A. Barone, F. Tafuri, High quality factor HTS Josephson junctions on low loss substrates. Supercond. Sci. Tech. **24**, 045008–045013 (2011)
88. D. Stornaiuolo, G. Rotoli, K. Cedergren, D. Born, T. Bauch, F. Lombardi, F. Tafuri, Submicron YBaCuO biepitaxial Josephson junctions: d-wave effects and phase dynamics. J. Appl. Phys. **107**, 113901–113606 (2010)
89. D. Stornaiuolo, G. Rotoli, D. Massarotti, F. Carillo, L. Longobardi, F. Beltram, F. Tafuri, Resolving the effects of frequency-dependent damping and quantum phase diffusion in $YBa_2Cu_3O_{7-x}$ Josephson junctions. Phys. Rev. B **87**, 134517 (2013)
90. E. Il'ichev, M. Grajcar, R. Hlubina, R.P.J. IJsselsteijn, H.E. Hoenig, H.-G. Meyer, A. Golubov, M.H.S. Amin, A.M. Zagoskin, A.N. Omelyanchouk, M.Yu. Kupriyanov, Degenerate ground

state in a mesoscopic $YBa_2Cu_3O_{7-x}$ grain boundary Josephson junction. Phys. Rev. Lett. **86**, 5369 (2001)
91. A.Y. Tzalenchuk, T. Lindström, S.A. Charlebois, E.A. Stepantsov, Z. Ivanov, A.M. Zagoskin, Mesoscopic Josephson junctions of high-Tc superconductors. Phys. Rev. B **68**, 100501 (2003)
92. E. Goldobin, D. Koelle, R. Kleiner, A.I. Buzdin, Josephson junctions with second harmonic in the current-phase relation: properties of $\varphi$ junctions. Phys. Rev. B **76**, 224523 (2007)
93. K. Inomata, S. Sato, K. Nakajima, A. Tanaka, Y. Takano, H.B. Wang, M. Nagao, H. Hatano, S. Kawabata, Macroscopic quantum tunneling in a d-wave high-Tc BiSrCaCuO superconductor. Phys. Rev. Lett. **95**, 107005 (2005)
94. X.Y. Jin, J. Lisenfeld, Y. Koval, A. Lukashenko, A.V. Ustinov, P. Mueller, Enhanced macroscopic quantum tunneling in BiSrCaCuO intrinsic Josephson-junction stacks. Phys. Rev. Lett. **96**, 177003 (2006)
95. P.A. Warburton, A.R. Kuzhakhmetov, G. Burnell, M.G. Blamire, H. Schneidewind, Decoupling of a current-biased intrinsic Josephson junction from its environment. Phys. Rev. B **67**, 184513 (2003)
96. A. Franz, Y. Koval, D. Vasyukov, P. Müller, H. Schneidewind, D.A. Ryndyk, J. Keller, C. Helm, Thermal fluctuations in ultrasmall intrinsic Josephson junctions. Phys. Rev. B **69**, 014506 (2004)
97. D. Vion, M. Götz, P. Joyez, D. Esteve, M.H. Devoret, Thermal activation above a dissipation barrier: switching of a small Josephson junction. Phys. Rev. Lett. **77**, 3435 (1996)
98. P. Joyez, D. Vion, M. Götz, M. Devoret, D. Esteve, The Josephson effect in nanoscale tunnel junctions. J. Supercond. **12**, 757–766 (1999)
99. M. Iansiti, A.T. Johnson, W.F. Smith, H. Rogalla, C.J. Lobb, M. Tinkham, Charging energy and phase delocalization in single very small Josephson tunnel junctions. Phys. Rev. Lett. **59**, 489 (1987); M. Iansiti, M. Tinkham, A.T. Johnson, W.F. Smith, C.J. Lobb, Charging effects and quantum properties of small superconducting tunnel junctions. Phys. Rev. B **39**, 6465 (1989)
100. J. Ankerhold, Overdamped quantum phase diffusion and charging effects in Josephson junctions. Europhys. Lett. **67**, 280–286 (2004)
101. U. Weiss, H. Grabert, Quantum diffusion of a particle in a periodic potential with ohmic dissipation. Phys. Lett. **108A**, 63–67 (1985)
102. J. Ankerhold, H. Grabert, P. Pechukas, Quantum Brownian motion with large friction. Chaos **15**, 026106–026115 (2005)
103. P. Hänggi, F. Marchesoni, Artificial Brownian motors: controlling transport on the nanoscale. Rev. Mod. Phys. **81**, 387 (2009)
104. L. Machura, M. Kostur, P. Talkner, J. Luczka, P. Hänggi, Quantum diffusion in biased washboard potentials: strong friction limit. Phys. Rev. E **73**, 031105 (2006)
105. B. Jäck, J. Senkpiel, M. Etzkorn, J. Ankerhold, C.R. Ast, K. Kern, Quantum Brownian motion at strong dissipation probed by superconducting tunnel junctions. Phys. Rev. Lett. **119**, 147702 (2017)
106. F.S. Bergeret, A.F. Volkov, K.B. Efetov, Odd triplet superconductivity and related phenomena in superconductor-ferromagnet structures. Rev. Mod. Phys. **77**, 1321 (2005)
107. A.I. Buzdin, Proximity effects in superconductor-ferromagnet heterostructures. Rev. Mod. Phys. **77**, 935 (2005)
108. M. Eschrig, Spin-polarized supercurrents for spintronics. Phys. Today **64**, 43–48 (2011)
109. J. Linder, J.W.A. Robinson, Superconducting spintronics. Nat. Phys. **11**, 307–315 (2015)
110. K. Senapati, M.G. Blamire, Z.H. Barber, Spin-filter Josephson junctions. Nat. Mater. **10**, 849–852 (2011)
111. A. Pal, Z.H. Barber, J.W.A. Robinson, M.G. Blamire, Pure second harmonic current-phase relation in spin-filter Josephson junctions. Nat. Commun. **5**, 3340 (2014)
112. A. Pal, K. Senapati, Z.H. Barber, M.G. Blamire, Electric field dependent spin polarization in GdN spin filter tunnel junctions. Adv. Mater. **25**, 5581 (2013)
113. A.K. Feofanov, V.A. Oboznov, V.V. Bol'ginov, J. Lisenfeld, S. Poletto, V.V. Ryazanov, A.N. Rossolenko, M. Khabipov, D. Balashov, A.B. Zorin, P.N. Dmitriev, V.P. Koshelets, A.V.

Ustinov, Implementation of superconductor/ferromagnet/ superconductor $\pi$-shifters in superconducting digital and quantum circuits. Nat. Phys. **6**, 593–597 (2010)
114. L. Trifunovic, Long-range superharmonic Josephson current. Phys. Rev. Lett. **107**, 047001–047005 (2011)
115. C. Richard, M. Houzet, J.S. Meyer, Superharmonic long-range triplet current in a diffusive Josephson junction. Phys. Rev. Lett. **110**, 217004–217008 (2013)
116. H. Sickinger, A. Lipman, M. Weides, R.G. Mints, H. Kohlstedt, D. Koelle, R. Kleiner, E. Goldobin, Experimental evidence of a $\varphi$ Josephson junction. Phys. Rev. Lett. **109**, 107002 (2012)
117. E. Goldobin, R. Kleiner, D. Koelle, R.G. Mints, Phase retrapping in a pointlike $\varphi$ Josephson junction: the butterfly effect. Phys. Rev. Lett. **111**, 057004–057007 (2013)
118. R. Menditto, H. Sickinger, M. Weides, H. Kohlstedt, M. Zonda, T. Novotný, D. Koelle, R. Kleiner, E. Goldobin, Phase retrapping in a $\varphi$ Josephson junction: onset of the butterfly effect. Phys. Rev. B **93**, 174506–174512 (2016)
119. I. Petković, M. Aprili, Phase dynamics of ferromagnetic Josephson junctions. Phys. Rev. Lett. **102**, 157003 (2009)
120. H. Courtois, Ph Gandit, D. Mailly, B. Pannetier, Long-range coherence in a mesoscopic metal near a superconducting interface. Phys. Rev. Lett. **76**, 130–133 (1996)
121. P. Dubos, H. Courtois, B. Pannetier, F.K. Wilhelm, A.D. Zaikin, G. Schön, Josephson critical current in a long mesoscopic S-N-S junction. Phys. Rev. B **63**, 064502–064507 (2001)
122. A.A. Golubov, M. Kupriyanov, E. Il'Ichev, The current-phase relation in Josephson junctions. Rev. Mod. Phys. **76**, 411 (2004)
123. D.S. Antonenko, M.A. Skvortsov, Quantum decay of the supercurrent and intrinsic capacitance of Josephson junctions beyond the tunnel limit. Phys. Rev. B **92**, 214513 (2015)
124. H. Courtois, M. Meschke, J.T. Peltonen, J.P. Pekola, Origin of hysteresis in a proximity Josephson junction. Phys. Rev. Lett. **101**, 067002 (2008)
125. A.V. Galaktionov, A.D. Zaikin, Fluctuations of the Josephson current and electron-electron interactions in superconducting weak links. Phys. Rev. B **82**, 184520–184525 (2010)
126. D. Massarotti, N. Banerjee, R. Caruso, G. Rotoli, M.G. Blamire, F. Tafuri, Electrodynamics of Josephson junctions containing strong ferromagnets. Phys. Rev. B **98**, 144516 (2018)
127. J.W.A. Robinson, J.D.S. Witt, M.G. Blamire, Controlled injection of spin-triplet supercurrents into a strong ferromagnet. Science **329**, 59–61 (2010)
128. G.-H. Lee, D. Jeong, J.-H. Choi, Y.-J. Doh, H.-J. Lee, Electrically tunable macroscopic quantum tunneling in a graphene-based Josephson junction. Phys. Rev. Lett. **107**, 146605 (2011)
129. L. Angers, F. Chiodi, G. Montambaux, M. Ferrier, S. Gureron, H. Bouchiat, J.C. Cuevas, Proximity dc squids in the long-junction limit. Phys. Rev. B **77**, 165408 (2008)
130. A.W. Kleinsasser, R.A. Buhrman, High-quality submicron niobium tunnel junctions with reactive-ion-beam oxidation. Appl. Phys. Lett. **37**, 841–843 (1980)
131. R.E. Miller, W.H. Mallison, A.W. Kleinsasser, K.A. Delin, E.M. Macedo, Niobium trilayer Josephson tunnel junctions with ultrahigh critical current densities. Appl. Phys. Lett. **63**, 1423–1425 (1993)
132. W.A. Little, Decay of persistent currents in small superconductors. Phys. Rev. **156**, 396–403 (1967)
133. J.S. Langer, V. Ambegaokar, Intrinsic resistive transition in narrow superconducting channels. Phys. Rev. **164**, 498 (1967); D.E. McCumber, B.I. Halperin, Time scale of intrinsic resistive fluctuations in thin superconducting wires. Phys. Rev. B **1**, 1054 (1970)
134. D.S. Golubev, A.D. Zaikin, Thermally activated phase slips in superconducting nanowires. Phys. Rev. B **78**, 144502 (2008)
135. N. Shah, D. Pekker, P.M. Goldbart, Inherent stochasticity of superconductor-resistor switching behavior in nanowires. Phys. Rev. Lett. **101**, 207001 (2008)
136. E. Hoskinson, Y. Sato, I. Hahn, R.E. Packard, Transition from phase slips to the Josephson effect in a superfluid $^4$He weak link. Nat. Phys. **2**, 23–26 (2006)
137. K.K. Likharev, Superconducting weak links. Rev. Mod. Phys. **51**, 101 (1979)

138. A.V. Galaktionov, D.S. Golubev, A.D. Zaikin, Andreev levels as a quantum dissipative environment. Phys. Rev. B **96**, 134509 (2017)
139. D.S. Golubev, A.D. Zaikin, Anomalous switching current distributions in superconducting weak links. IEEE Trans. Appl. Supercond. **28**, 1–5 (2018)
140. N. Giordano, Evidence for macroscopic quantum tunneling in one-dimensional superconductors. Phys. Rev. Lett. **61**, 2137 (1988)
141. A. Bezryadin, *Superconductivity in Nanowires* (Wiley, New York, 2012)
142. H. Bartlof, *Fluctuation Mechanisms in Superconductors* (Wiley, New York, 2015)
143. A. Bezryadin, C.N. Lau, M. Tinkham, Quantum suppression of superconductivity in ultrathin nanowires. Nature **404**, 971–974 (2000); C.N. Lau, N. Markovic, M. Bockrath, A. Bezryadin, M. Tinkham, Quantum phase slips in superconducting nanowires. Phys. Rev. Lett. **87**, 217003 (2001); M. Tinkham, J.U. Free, C.N. Lau, N. Markovic, Hysteretic I-V curves of superconducting nanowires. Phys. Rev. B **68**, 134515 (2003); A. Rogachev, A.T. Bollinger, A. Bezryadin, Influence of high magnetic fields on the superconducting transition of one-dimensional Nb and MoGe nanowires. Phys. Rev. Lett. **94**, 017004 (2005)
144. F. Altomare, A.M. Chang, M.R. Melloch, Y. Hong, C.W. Tu, Evidence for macroscopic quantum tunneling of phase slips in long one-dimensional superconducting Al wires. Phys. Rev. Lett. **97**, 017001 (2006); Y. Chen, Y.-H. Lin, S.D. Snyder, A.M. Goldman, A. Kamenev, Dissipative superconducting state of non-equilibrium nanowires. Nat. Phys. **10**, 567–571 (2014)
145. M. Sahu, M.H. Bae, A. Rogachev, D. Pekker, T.C. Wei, N. Shah, P.M. Goldbart, A. Bezryadin, Individual topological tunnelling events of a quantum field probed through their macroscopic consequence. Nat. Phys. **5**, 503–508 (2009)
146. P. Li, P.M. Wu, Y. Bomze, I.V. Borzenets, G. Finkelstein, A.M. Chang, Switching currents limited by single phase slips in one-dimensional superconducting Al nanowires. Phys. Rev. Lett. **107**, 137004 (2011)
147. P. Li, P.M. Wu, Y. Bomze, I.V. Borzenets, G. Finkelstein, A.M. Chang, Retrapping current, self-heating, and hysteretic current-voltage characteristics in ultranarrow superconducting aluminum nanowires. Phys. Rev. B **84**, 184508 (2011)
148. X.D.A. Baumans, V.S. Zharinov, E. Raymenants, S.B. Alvarez, J.E. Scheerder, J. Brisbois, D. Massarotti, R. Caruso, F. Tafuri, E. Janssens, V.V. Moshchalkov, J. Van de Vondel, A.V. Silhanek, Statistics of localized phase slips in tunable width planar point contacts. Sci. Rep. **7**, 44569 (2017)